

1  
2  
3  
4  
5  
6  
7  
8  
9  
10  
11  
12  
13  
14  
15  
16  
17  
18  
19  
20  
21  
22  
23  
24  
25  
26  
27

**Numerical investigation of the refractive properties of near-horizontal shore platforms and their effects on harmonic and stationary wave patterns**

**R. Krier-Mariani<sup>1</sup>, W. Stephenson<sup>1</sup>, S. Wakes<sup>2</sup>, M. Dickson<sup>3</sup>**

<sup>1</sup> School of Geography, University of Otago, New Zealand

<sup>2</sup> Department of Mathematics and Statistics, University of Otago, New Zealand

<sup>3</sup> School of Environment, University of Auckland, New Zealand

**Corresponding author:** Raphael, Krier-Mariani ([raphael.m.krier@gmail.com](mailto:raphael.m.krier@gmail.com); [raphael.krier@postgrad.otago.ac.nz](mailto:raphael.krier@postgrad.otago.ac.nz))

28 **Key Points:**

- 29
- Through refraction, concave and convex near-horizontal shore platforms can separate the frequency components of the wavefield.
- 30
- Refraction patterns controlled by platform edge convexity affect the dominance of wind, swell and infragravity waves across platforms.
- 31
- Coherent amplification from the intersection of refracted infragravity waves
- 32
- controls the nodal state of alongshore stationary waves.
- 33
- 34

35 **Abstract**

36 Near-horizontal shore platforms display highly irregular plan shapes, but little is  
37 known about the way in which these irregularities influence the significant wave height ( $\widehat{H}_s$ )  
38 on the platforms and the frequency components of the nearshore wavefield. We use a non-  
39 linear Boussinesq wave model to conduct harmonic and bispectral mode decomposition  
40 analyses, studying the control of concave and convex platform edges over wind (WW: 0.125  
41 - 0.33 Hz), swell (SW: 0.05 - 0.125 Hz) and infragravity (IG: 0.008 - 0.05 Hz) frequencies. For  
42 breaking and non-breaking waves, increasing the platform edge concavity intensified wave  
43 divergence and subsequent attenuation of SW and IG across the outer platforms, reducing  $\widehat{H}_s$   
44 by up to 25%. Increasing the platform edge convexity intensified focusing and amplification  
45 of SW and WW over the outer platforms, increasing  $\widehat{H}_s$  by up to 18% and 55% for breaking  
46 and non-breaking waves. In the presence of breaking, IG amplification depended on the  
47 generation of wave divergence across the inner platform, a condition determined by a critical  
48 convex curvature threshold ( $|\mathcal{K}|=1.8$ ) balancing wave focusing from refraction and  
49 defocusing from breaking. We find that convex curvature can determine the relative  
50 dominance of WW, SW and IG across platforms. Alongshore, coherent wave interactions  
51 governed IG stationary patterns defined by a node near the platform centreline and two  
52 antinodes on either side of concave edges. A node was generated at the platform centreline,  
53 and two antinodes were observed on either side of the convex edges for  $|\mathcal{K}|>1.8$ , with the  
54 opposite pattern observed for  $|\mathcal{K}|<1.8$ .

55

56 **Plain Language Summary**

57 Near-horizontal shore platforms fronting coastal cliffs act as wave energy buffers,  
58 regulating wave-induced erosion in rock coast environments. Genuine research endeavours  
59 have permitted establishing the link between near-horizontal platform morphology and wave  
60 transformation across-shore. However, the effects of alongshore variations in near-horizontal  
61 platform morphology on the properties of nearshore wavefields remain sparsely  
62 documented. As ocean waves share akin refractive properties to light rays, it can be assumed  
63 that, similarly to optical lenses, shore platforms can separate waves according to their  
64 frequency depending on their geometry. Subsequently, the convergence and divergence of  
65 refracted wave trains of similar phases and frequencies could affect the properties of the  
66 nearshore wavefield. The present research investigates this phenomenon over concave and  
67 convex edge platforms and its impact on the nearshore wavefield characteristics. Our results  
68 show that wave refraction over near-horizontal platforms with concave and convex edges  
69 affects the relative dominance of short, medium and long-period waves across shore and  
70 results in alongshore stationary wave patterns near the shoreline with nodal states varying in  
71 relation to platform edge geometry. Such patterns likely result in alongshore variations in  
72 wave erosion and the generation of wave-generated currents shaping rock coasts in the  
73 platform.

74  
75  
76  
77

78 **1 Introduction**

79 Near-horizontal shore platforms, defined by a low gradient ( $\tan\beta < 0.0175$ ) and a  
80 steep seaward edge, are prevailing coastal landforms in rock coast environments (Sunamura,  
81 1992; Trenhaile, 1999). These landforms have an essential role in wave transformation  
82 processes, regulating wave erosive forces at the shoreline (Stephenson and Kirk, 2000;  
83 Matsumoto et al., 2016a,b). Thus, an accurate description of the geomorphic control exerted  
84 by shore platforms on nearshore wave transformation patterns is necessary for improving  
85 rock coast geomorphological models.

86 Studies have investigated the control of near-horizontal shore platform morphology on  
87 the cross-shore evolution of the wavefield (e.g. Beetham and Kench, 2011; Marshall and  
88 Stephenson, 2011; Ogawa et al., 2016). Wave breaking induced by the sharp depth transition  
89 at the seaward edge of a platform results in the dissipation of incident swell waves (SW: 0.05  
90  $\text{Hz} < f < 0.125 \text{ Hz}$ ) and the generation of low-frequency infragravity waves (IG:  $f < 0.05 \text{ Hz}$ )  
91 over the platform (Poate et al., 2020). Across the platform surface, IG gradually amplify due  
92 to shoaling and energy is transferred from high to lower frequencies, becoming the dominant  
93 frequency component over the inner platform (Beetham and Kench, 2011; Marshall and  
94 Stephenson, 2011; Ogawa et al., 2011). Wind waves (WW:  $0.125 < f < 0.33 \text{ Hz}$ ) can propagate  
95 onto platforms from offshore and, in some cases, be locally generated over the outer platform  
96 to become the dominant frequency component in this area (Marshall and Stephenson, 2011;  
97 Ogawa et al., 2011). These observations were summarised in the conceptual model of Ogawa  
98 et al. (2011), indicating that it is common for the outer platform, platform centre, and inner  
99 platform to be dominated by WW, SW and IG, respectively. Ogawa et al. (2011) suggested  
100 that these zones shift across-shore with tidal elevation and showed that the relative  
101 submergence of shore platforms (depth at the seaward edge/incident wave height) is a critical  
102 factor controlling the relative dominance of SW and IG. Collectively, understanding the  
103 behaviour of each frequency band of the wavefield helps to depict the variation of significant  
104 wave height ( $H_s$ ) across platforms affecting erosion of the platform and cliff (Trenhaile,  
105 2000). However, the impact of shore platform morphology on two-dimensional wave  
106 transformation processes and effect on the frequency bands composing the wavefield have  
107 been overlooked.

108 Few field studies have considered the impact of the platform morphology of near-  
109 horizontal platforms on two-dimensional wave transformation patterns (Krier-Mariani et al.  
110 2022, 2023). Krier-Mariani et al. (2023) showed that directional patterns controlled by  
111 irregularities in platform morphology generated localised areas of wave ray convergence and  
112 divergence as well as alongshore variations in standing IG patterns, influencing the wave  
113 energy distribution over the platform surfaces. Based on these observations, Krier-Mariani et  
114 al. (2023) introduced a conceptual model in which concave and convex platform edge  
115 geometries would control wave ray convergence and divergence patterns over the platform  
116 surface, subsequently affecting the IG energy levels and SW decay rates. However, the

117 influence of platform edge geometry on two-dimensional wave patterns could not be clearly  
118 isolated from field observations.

119 In the absence of detailed field studies on the effects of platform edge geometry on  
120 wave transformation characteristics, the literature on morphologically analogous submerged  
121 flat structures is useful. Depending on their geometry, submerged flats can separate the  
122 frequency components of the wavefield, refracting and reorganising the wave crests of  
123 incident waves according to their frequency (Jarry et al., 2011; Griffiths and Porter, 2012; Li  
124 et al., 2020). This phenomenon can result in complex refraction patterns specific to each  
125 frequency component of the wavefield, leading to the generation of caustic rays (clusters of  
126 caustic points generated by wave ray intersection) over submerged surfaces (e.g. Mandlier  
127 and Kench, 2012). Patterns of wave ray convergence and divergence induced by refraction  
128 over submerged flat structures significantly impact the wavefield characteristics. Wave ray  
129 convergence results in a localised enhancement of wave height (e.g. Ito and Tanimoto, 1972;  
130 Berkhoff et al., 1982), skewness and kurtosis (Janssen and Herbers, 2009; Jarry et al., 2011;  
131 Lawrence et al., 2022) while wave ray divergence has the opposite effects.

132 Although relatively few studies have considered the impact of submerged flat  
133 geometries on the cross-shore evolution of harmonic and subharmonic components of the  
134 wavefield, harmonic components amplification has been observed in areas of wave  
135 convergence (e.g. Lynett and Liu, 2004; Gouin et al., 2017). According to Li et al. (2020), this  
136 phenomenon could be attributed to the non-linear effects of convergence on wave height  
137 amplification. As the geometry of submerged flats influences the cross-shore pattern of wave  
138 convergence (intensity and location) of each harmonic, it likely also influences the cross-shore  
139 patterns of wave harmonics amplification, intrinsically affecting the dominance of different  
140 wave frequencies across platforms. This hypothesis as yet to be verified.

141 It has proven difficult to establish causality between patterns of wave ray intersection,  
142 increased nonlinearity and alongshore wave height amplification for random wavefields,  
143 notably due to the limitation of wave ray tracking techniques to evaluate complex wave ray  
144 crossing patterns in dense constellations of caustics (Ito and Tanimoto, 1972). Another way  
145 of approaching this problem involves considering the impact of coherent wave interaction  
146 patterns on the amplification of dominant frequency components of the wavefield. Coherent

147 wave interaction refers to the non-linear process occurring at the intersection of waves with  
148 similar frequency, waveform and phase. It has been identified as a fundamental non-linear  
149 wave amplification process in optics (e.g. Young, 1802), quantum mechanics (e.g., Weiland  
150 and Wihelmsson, 1977; Falk, 1979; Inouye et al., 1999; Kozuma et al., 1999) and geoscience  
151 (e.g. Harid et al., 2014). There have been few investigations of this process in coastal wave  
152 studies, but Dalrymple (1975) demonstrated that this process could result in the formation of  
153 alongshore stationary wave patterns in random wavefields and the subsequent formation of  
154 nearshore currents. More recently, Tamura et al. (2020) showed that, similar to light  
155 refraction through a prism, ocean wave refraction over a submarine canyon could separate  
156 waves of a random wavefield according to their frequency and phase, favouring coherent  
157 wave interactions. Based on this theoretical grounding, it is hypothesised that by controlling  
158 the refraction patterns of individual frequency components of the wavefield, submerged flat  
159 (e.g. shore platforms) geometry affects coherent wave amplification over submerged flat  
160 surfaces, leading to the generation of alongshore stationary wave patterns for SW and IG.

161 The impact of shore platform geometry on the behaviour of wave harmonics and  
162 stationary wave patterns remains to be evaluated in detail on near-horizontal platform  
163 surfaces. However, such a task was proven to be difficult during field observations due to the  
164 variable nature of nearshore wavefields and the morphological complexity of shore platforms  
165 (e.g. Krier-Mariani et al. 2022, 2023). Therefore, this study adopts a numerical modelling  
166 approach to address the question: How do mesoscale variations in platform edge geometry  
167 affect the behaviour of wave harmonics and the subsequent wave height distribution across  
168 and along platform surfaces?

## 169 **2 Method**

### 170 **2.1 Model set up**

171 The phase-resolving Boussinesq wave model FUNWAVE\_TVD V3.6 (Shi et al., 2012)  
172 was used to investigate two-dimensional wave transformation over shore platforms. This  
173 model treats wave transformation in the time domain and provides a robust representation  
174 of non-linear processes, refraction and diffraction while retaining information on the wave

175 phase (Sheremet et al., 2011; Buckley et al., 2015, Buckley et al., 2018; Thomas and  
176 Dwarakish, 2015).

177

### 178 **2.1.1 Domain**

179 Idealised three-dimensional near-horizontal platform morphologies were incorporated  
180 into a 1274 m (x-axis) to 300 m (y-axis) domain (Fig. 1a). A 0.35 m deep, 250 m wide shallow  
181 planar surface was included at the landward extremity to absorb wave energy and minimise  
182 resonance. The platforms were defined by a constant gradient of 0.35 degrees, a width of 300  
183 m (at the centreline,  $y = 150$  m) and a 3m high seaward cliff of 45 degrees. The nearshore  
184 bathymetry profile was composed of a 480 m subtidal ramp (at the centreline) with a gradient  
185 of 0.35 degrees followed by an 8 m deep and 635 m wide flat.

186 Planform geometry was represented using three generic edge geometries defined as  
187 straight, concave and convex. The degree of curvature of the concave ( $\mathcal{K} < 0$ ) and convex  
188 ( $\mathcal{K} > 0$ ) edge geometries was derived from the parametric ellipse equation. The semi-major  
189 axis ( $a$ , along the x-axis) was kept constant (120 m) to avoid modifying the cross-shore profile  
190 along the centreline, and various degrees of edge curvature were obtained from 2 m  
191 increments along the semi-minor axis ( $b$ , along the y-axis) between 50 to 100 m, resulting in  
192 26 cases with edge curvatures ( $|\mathcal{K}| = |a/b|$ ) ranging from 1.2 to 2.4 (Fig. 1b-f). The  
193 bathymetry was smooth to reduce noise generated by sharp edges and interpolated to a 2 m  
194 grid adopted to ensure model stability following a series of sensitivity analyses, providing a  
195 realistic representation of model resolution used in previous research in nearshore areas (e.g.  
196 Su et al., 2021).

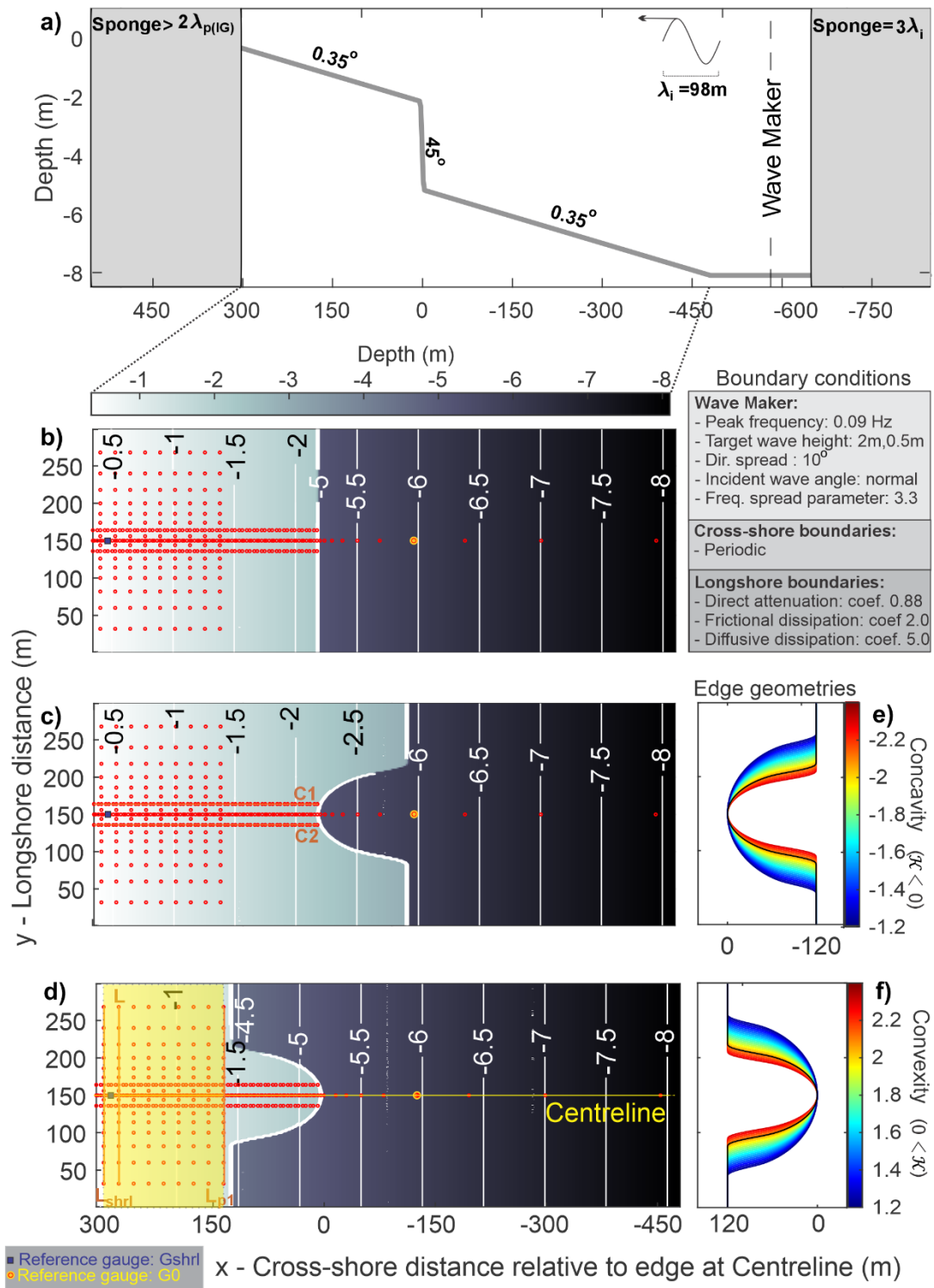


**Figure 1:** Boussinesq wave model configuration showing the bathymetry profile along the centreline ( $y = 150\text{m}$ ) (a), the model domain for the straight, concave and convex platforms (b-d), and the range of platform edge curvatures considered (e,f). Specifications of the boundary conditions are annotated in the figure. The red dots mark the location of the virtual gauges used for analysis. The yellow shaded area (between  $L_p$  and  $L_{srl}$ ) represents the inner platform section considered for alongshore analysis.

197 **2.1.2 Wave conditions**

198 The model was forced by irregular waves with a directional spread of 10 degrees. An  
199 internal wavemaker (Wei et al., 1999) was located on the deep flat at the bottom of the  
200 subtidal ramp, five wavelengths ( $\lambda_i$ ) away from the platform edge to avoid distortion of the  
201 initial wave crests. Irregular waves were generated using a JONSWAP wave spectra  
202 (Hasselmann et al., 1973) with a fixed peak enhancement factor of 3.3, a peak frequency ( $f_p$ )  
203 of 0.09 Hz and direction of 0° (shore-normal) to simplify the visualisation of the refraction  
204 effects induced by different platform edge geometries.

205 Two sets of simulations were generated to investigate the transformation of: (1) waves  
206 propagating across the platform surface without breaking ( $H_s= 0.5$  m), as such waves can  
207 release large amounts of erosive energy when they break against cliffs (Thompson et al.,  
208 2019; Thompson et al., 2022); and (2) wave breaking at the seaward edge ( $H_s= 2$  m) decaying  
209 across the platform, which are typically used to define variation of wave erosive force across  
210 platforms in geomorphological models (e.g. Trenhaile, 2000; Matsumoto et al., 2016a,b).  
211 These two sets of simulations combined with the range of platform concave and convex  
212 curvatures resulted in 106 simulations (including straight edge reference cases). The default  
213 breaking index of FUNWAVE-TVD ( $\gamma_b=0.80$ ) was used to represent wave breaking, providing  
214 a close representation of the breaking conditions for steep submerged slopes (Blenkinsopp  
215 and Chaplin, 2008). The effects of bottom friction were not considered (i.e. the frictional  
216 dissipation coefficient was set to  $C_d= 0.002$ , representing a smooth surface).

217

218 **2.1.3 Boundary conditions**

219 The domain boundary conditions were defined to minimise reflection. Periodic  
220 boundaries (Chen et al., 2003) were applied to the northern and southern extremities of the  
221 domain, allowing waves to propagate out of the domain. Following Shi et al. (2016), sponge  
222 layers employing a direct damping coefficient as well as dissipation by friction and diffusion  
223 were used to reduce noise and dampen wave energy at the eastern and western sides of the  
224 domain (Fig. 1a). The width of the sponge layer at the shallow western side of the domain  
225 was chosen to correspond to twice the peak wavelength of the IG at this location (estimated

226 during trial runs using the virtual gauge  $G_{shrl}$  at the shoreline, Fig. 1), to avoid reflection and  
227 the subsequent generation of standing IG waves.

228

#### 229 **2.1.4 Model Validation**

230 Due to the lack of two-dimensional field measurements in similar near-horizontal  
231 shore platform settings, no direct validation of our model simulations was carried out.  
232 However, a number of studies validated FUNWAVE-TVD against field observations over coral  
233 reefs, proving the model's ability to represent wave transformation over smooth submerged  
234 flats with sharp seaward edges (e.g. Mendonca et al., 2008; Su et al., 2015; Zhang et al., 2019).  
235 As the present study explores wave processes such as refraction and non-linear energy  
236 transfer fairly well represented by the model (Griffiths and Porter, 2012; Su et al., 2015) and  
237 does not investigate subsequent processes such as wave-driven circulation and sediment  
238 transport, it is deemed unnecessary to validate the model with experimental data at this stage  
239 (similar inference were made in da Silva et al., 2023).

#### 240 **2.2 Measurements and analysis**

241 To determine the impact of planform geometries on wave transformation across the  
242 platforms, the spectral evolutions of waves propagating across concave and convex platforms  
243 (affected by two-dimensional transformation processes) were compared to the spectral  
244 evolution of waves propagating across the straight-edge platform (only affected by on-  
245 dimensional transformation processes). This approach permitted the identification of spectral  
246 anomalies representing the energy variations for specific harmonics induced by refraction.  
247 Positive and negative anomalies indicate harmonic amplifications and attenuation,  
248 respectively. Combined, the harmonic anomalies result in anomalies of significant wave  
249 height across platforms ( $\Delta\widehat{H}_s$ ). Following Baldock et al. (2020), the cross-shore patterns of  
250  $\Delta\widehat{H}_s$  were then compared to the directional patterns along the platform centrelines to identify  
251 the effects of refraction patterns controlled by platform edge geometry on significant wave  
252 height distribution across platforms.

253 In the alongshore, the effects of coherent wave interaction induced by refraction over  
254 concave and concave platforms on the generation of stationary wave patterns were

255 considered. For this purpose, the bispectrum (Hasselmann et al., 1963) provides a convenient  
256 representation of the wavefield as it holds information on the wave phase, frequency and  
257 power necessary to detect phase coupling. The bispectrum, defined from the third moment  
258 of the free surface elevation time series, also represents a measure of skewness, which  
259 increases in areas of wave ray intersection (Janssen and Herbers, 2009; Jarry et al., 2011;  
260 Lawrence et al., 2022). Following Kim and Powers (1979), who investigated the impact of  
261 coherent interactions of random electromagnetic waves on plasma density fluctuation using  
262 bispectral properties, the frequency, phase and power information yielded by the bispectrum  
263 were used to identify patterns of coherent wave interactions over the inner platforms. A  
264 modal decomposition method based on bispectral properties (Appendix 2), the Bispectral  
265 Mode Decomposition or BMD (Schmidt, 2020), was employed to identify the modal state of  
266 coherent structures for self-interacting harmonic components within the SW and IG  
267 frequency bands. The areas of coherent wave interactions were then compared to the wave  
268 height distribution of SW and IG over platforms of various geometries to identify patterns of  
269 coherent wave amplification.

270

### 271 **2.2.1 Wave measurements**

272 Wave records were obtained from virtual gauges recording surface elevation ( $\eta$ ) as  
273 well as  $u$  and  $v$  velocity components at 2 Hz (Fig. 1b-d). In the cross-shore direction, the gauge  
274 spacing along the centreline increased seaward from the platform edge (increment based on  
275 geometric series starting with a spacing of 4 m with an increment factor of 1.5). On the  
276 platforms, the gauge spacing was irregular but not exceeding 6 m along the centreline,  
277 transects  $C_1$  and  $C_2$ . The distance between the gauges composing the alongshore transects  
278 (between  $L_0$  and  $L_{shrl}$ ) increased on either side of the centreline from 6 to 30 m (with an  
279 increment factor of 1.25). Statistical analyses of the wavefield properties were based on an  
280 observation window of 2048 seconds, starting 230 seconds after the start of the simulations,  
281 marking the time at which SW reached the landward extremity of the domain and IG were  
282 generated.

283

### 284 2.2.2 Definition of wave height

285 The significant wave height ( $H_s$ ) was defined from the spectra moment (e.g. Thornton  
286 and Guza, 1983):

$$H_s = 4 \sqrt{\int_{f_{min}}^{f_{max}} S(f) \cdot df} \quad (1)$$

287

288 The wave spectra estimates  $S(f)$  were generated using the Welch (1967) method with  
289 segment lengths of 512 samples, 50% overlap and a Hanning window resulting in 20 Degrees  
290 of Freedom (Priestley, 1981). To provide a more detailed representation of the wavefield, the  
291 gravity and infragravity waves were further divided into two frequency bands, encapsulating  
292 the dominant harmonics observed within the WW, SW, and IG (high and low) frequency  
293 ranges across the domain (Table 1). The wave height associated with each of these frequency  
294 bands was determined using:

295

$$H_{f_{np}} = 4 \sqrt{\int_{f_{low}}^{f_{high}} S(f) \cdot df} \quad (2)$$

296 where  $n$  denotes the rank of the harmonic,  $f_{low}$  and  $f_{high}$  represents the lower and higher  
297 frequencies of the power spectral density peak associated with this harmonic, Table 1. The  
298 reference incident wave height ( $H_0$ ) was defined from measurements taken at the gauge  $G_0$   
299 located at the top of the subtidal ramp (Fig. 1) and was used to normalise the wave height on  
300 the platform surface ( $\widehat{H}_s(x) = H_s(x)/H_0$ ,  $\widehat{H}_{f_{np}}(s) = H_{f_{np}}(x)/H_0$ ). For simplicity,  
301 normalised wave heights are hereafter referred to as wave heights.

302

303

304

305

306

307

308

309 **Table 1** Frequency band analysis parameters

Conventional Frequency class	Frequency subclass	Corresponding Harmonic	Frequency ( $f_{np}$ )	Frequency range ( $f_{low} - f_{high}$ )
Gravity waves	Wind waves (WW)	Second harmonic	$f_{2p}$	0.15 – 0.20 Hz
	Swell waves (SW)	Principal harmonic	$f_p$	0.06 – 0.12 Hz
Infragravity waves	Infragravity High (IG <sub>H</sub> )	Second subharmonic	$f_{1/2p}$	0.04 – 0.05 Hz
	Infragravity Low* (IG <sub>L</sub> )	Fifth subharmonic	$f_{1/5p}$	0.008 – 0.03 Hz

310 \*Note that the typical cutoff frequency for the lower portion of the IG frequency band is 0.005 Hz (e.g. Pequignet et al., 2014;  
 311 Gawehn et al., 2016). However, the chosen cutoff frequency of 0.008 Hz is more appropriate to describe the low IG in the  
 312 simulated wavefield as it corresponds to a trough in the power spectra estimate across the entire domain, which provides a  
 313 better physical representation of the low IG.  
 314

### 315 2.2.3 Definition of peak direction

316 The angle  $\alpha$  between the peak direction of waves propagating on either side of the  
 317 centreline (along the cross-shore transects C1 and C2, Fig. 1) was used to investigate the  
 318 evolution of wave convergence and divergence along the platform centrelines. The peak  
 319 direction of waves over the platform was estimated from the directional wave spectra  
 320  $S(f, \theta) = S(f)G(\theta|f)$  calculated from the free surface elevation ( $\eta$ ) and velocity  
 321 components ( $u$  and  $v$ ) time series by applying the Extension of the Maximum Entropy  
 322 Principle (EMEP) method (Hashimoto et al., 1994). To this effect, segments of 512 samples  
 323 were used to estimate the frequency spectra ( $S(f)$ ) and 200 iterations to define the  
 324 approximation of the spreading function ( $G(\theta|f)$ ) resulting in 76 frequency bins and  
 325 directional bins of 5°.

326

### 327 2.2.4 Identification of coherent wave interaction patterns

328 The BMD was applied to the free surface elevation time series recorded by the two-  
 329 dimensional virtual gauge array between  $L_p$  and  $L_{shrl}$ , marking the boundaries of the spatial  
 330 domain  $\xi$  (Fig. 1). The welch periodograms employed in the BMD were computed using  
 331 segments of 512 samples, 50% overlap and a Hanning window resulting in 20 Degrees of  
 332 Freedom. Patterns of coherent wave interactions were identified from coherent self-

333 interaction maps ( $\psi_{k,k}$ ) which are defined by the product of cross-frequency fields  $\phi_{k \circ k}$  and  
 334 the bispectral modes  $\phi_{k+k}$  obtained from the BMD:

$$\psi_{k,k}(\xi, f_k, f_k) = |\phi_{k \circ k} \circ \phi_{k+k}| \quad (3)$$

335  
 336 where the frequency  $k$  considered were  $f_p$  and  $f_{1/5p}$ , representing the dominant harmonics  
 337 in the SW and IG frequency bands. The cross-frequency fields  $\phi_{k \circ k}$  are maps of phase  
 338 alignment for these frequencies, while bispectral modes  $\phi_{k+k}$  represent the amplitude of  
 339 oscillations of the sea surface at frequency  $2k$ . Conventionally, the largest values of the  
 340 normalised coherent self-interaction maps  $\widehat{\psi}_{k,k}$  indicate areas where phase coupling has the  
 341 strongest effect on wave amplitude for the sum frequency  $2k$ . The interaction maps for  
 342 straight wave crests with parallel wave rays are expected to be homogeneous alongshore. In  
 343 contrast, for cases where wave crests are bent and wave rays intersect, interaction maps will  
 344 be non-homogenous alongshore and display maxima in areas of wave ray intersection. In the  
 345 presence of coherent wave amplification, maxima in coherent self-interaction maps  
 346 correspond to areas of wave height amplification at frequency  $k$ .

347

### 348 **3 Results**

#### 349 **3.1 Impact of planform geometry on across-shore wave transformation**

##### 350 **3.1.1 Non-breaking waves ( $H_0 = 0.5$ m)**

351 The spatial evolution of the spectral properties of non-breaking waves propagating  
 352 across the domain was examined for the three types of platform geometries (Fig. 2), for which  
 353 the power spectra density was concentrated around four distinctive frequency components  
 354 (Fig. 2a): the second and the principal harmonics ( $f_{2p}$  and  $f_p$ ) within the WW and SW  
 355 frequency bands; and the second and fifth subharmonics ( $f_{1/2p}$  and  $f_{1/5p}$ ) within the IG<sub>H</sub> and  
 356 IG<sub>L</sub> frequency bands.

357 The spectral anomalies observed over the concave platforms indicated an attenuation  
 358 of the principal harmonic (Fig. 2b-e). This phenomenon intensified with increasing degrees of  
 359 curvature (with minimum spectral anomalies at peak frequency reducing from  $-0.09$  m<sup>2</sup> Hz<sup>-1</sup>

360 at  $|\mathcal{K}|= 1.2$  to  $-0.41\text{m}^2 \text{ Hz}^{-1}$  at  $|\mathcal{K}|= 2.4$ ). In contrast, an amplification of the second and  
361 principal harmonics was observed across convex platforms (Fig. 2g-j), intensifying with  
362 increasing edge curvature (with maximum spectral anomalies at peak frequency increasing  
363 from  $0.52 \text{ m}^2 \text{ Hz}^{-1}$  at  $\mathcal{K}= 1.2$  to  $1.37 \text{ m}^2 \text{ Hz}^{-1}$  at  $\mathcal{K}= 2.4$ ).

364 The variation of spectral characteristics of each harmonic over the concave and convex  
365 platforms can be expressed in terms of mean wave height anomalies ( $\overline{\Delta H_{f_{np}}}$ ). The most  
366 significant impacts of platform curvature on mean wave height anomalies were observed  
367 within the WW and SW frequency bands. The mean wave height anomalies associated with  
368 the second and the principal harmonics displayed a very strong linear dependency ( $R^2 > 0.9$ )  
369 to the degree of platform edge curvature (Fig. 2f,k). The increase of curvature from  $|\mathcal{K}|= 1.2$   
370 to 2.4 promoted the attenuation of harmonics within the WW and SW frequency bands across  
371 concave platforms and the amplification of these waves across convex platforms. The  
372 attenuation of the second and principal harmonics across concave platforms of high curvature  
373  $|\mathcal{K}|= 2.4$  corresponded to 9% and 15% of  $H_0$ . Across convex platforms of high curvature,  $|\mathcal{K}|=$   
374 2.4, the amplification of the second and principal harmonics reached up to 11% and 29% of  
375  $H_0$ . The mean wave height anomalies for the subharmonic in the  $\text{IG}_H$  and  $\text{IG}_L$  frequency bands  
376 were negligible for nonbreaking waves.

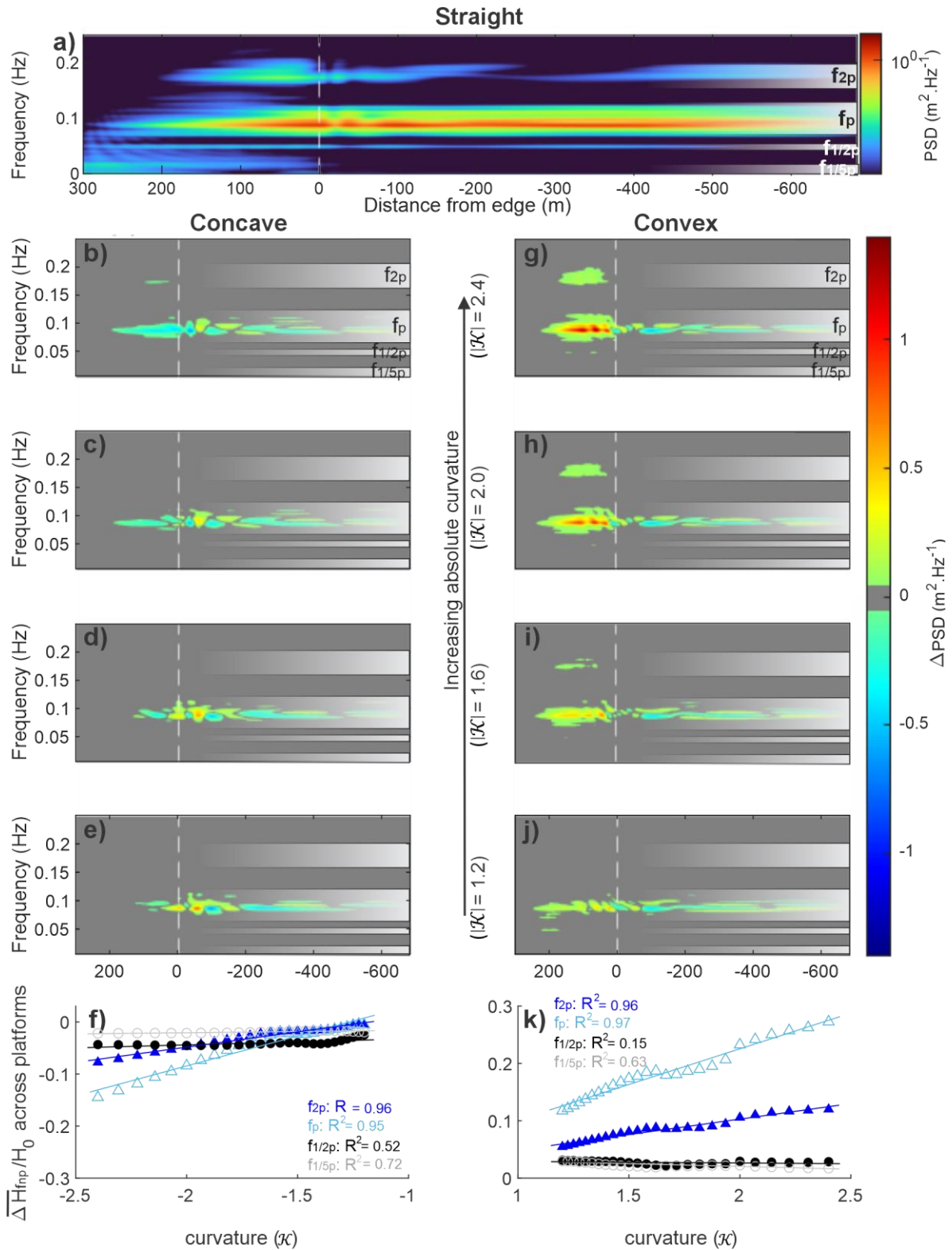


**Figure 2:** Impact of platform edge curvature on the harmonic components of the wavefield for non-breaking waves showing: the spectral anomalies in relation to the straight edge platform (a) for concave platform geometries (b-e) and convex platform geometries (g-j); and the impact of curvature on the mean wave height of each harmonic across the concave (f) and convex (k) platforms.

377

378

379  $\Delta\widehat{H}_s$  across the platform can be assumed to be impacted by refraction patterns  
380 controlled by platform geometry. To explore this process, directional patterns and  $\Delta\widehat{H}_s$  across  
381 the centrelines of each platform were compared for various edge curvatures. The cross-shore  
382 patterns of  $\Delta\widehat{H}_s$  presented in Fig. 3a,b were modulated by the platform edge curvature, with  
383 magnitude increasing with curvature for both types of platform geometries. As a result, for  
384 high degrees of curvature ( $|\mathcal{K}| = 2.4$ ), the negative anomalies across the concave platforms  
385 indicated a maximum of 25% attenuation in significant wave height (Fig. 3a), while the  
386 positive anomalies across the convex platforms (Fig. 3b) indicated a 55% amplification of  
387 significant wave height. The location of the largest  $\Delta\widehat{H}_s$  shifted across platforms in relation  
388 to curvature. For concave platforms, the largest negative  $\Delta\widehat{H}_s$  over the outer platform shifted  
389 landward with decreasing curvature from  $|\mathcal{K}| = 2.4$  to 1.9. Similarly, the largest positive  $\Delta\widehat{H}_s$   
390 across the convex platforms shifted landward, reaching the inner platform for  $|\mathcal{K}| < 1.6$ . For  
391 low degrees of concave curvatures ( $|\mathcal{K}| < 1.9$ ), corresponding to curvatures for which  
392 amplification of wave energy seaward of the platform edge was observed (Fig. 2b-e), wave  
393 transformation patterns across the platform centreline were affected by the preconditioning  
394 of incident waves occurring off the platform edge. Therefore, the description of the following  
395 results focuses on concave edge curvatures,  $|\mathcal{K}| > 1.9$ .

396 Similarly to the cross-shore evolution of  $\Delta\widehat{H}_s$ , the peak magnitude of wave ray  
397 divergence observed across concave platforms and convergence across the convex platforms  
398 decreased and shifted landward from the mid-platform ( $x \approx 150$  m) to the outer platform  
399 with decreasing curvature (Fig. 3c,d). A Spearman rank correlation (Fig. 3e,f) revealed that the  
400 dependency of cross-shore  $\Delta\widehat{H}_s$  on the directional patterns observed over the concave  
401 platforms was only relevant (moderate to strong,  $\rho_s > 0.4$ ) for platform edge curvatures  
402 exceeding 1.9. In contrast, a strong relationship ( $\rho_s > 0.6$ ) as observed between wave height  
403 anomaly and directional patterns over convex platforms for the majority of platform edge  
404 curvatures, indicating that  $\Delta\widehat{H}_s$  across the convex platforms were predominantly controlled  
405 by the wave convergence and divergence across the centreline.

406

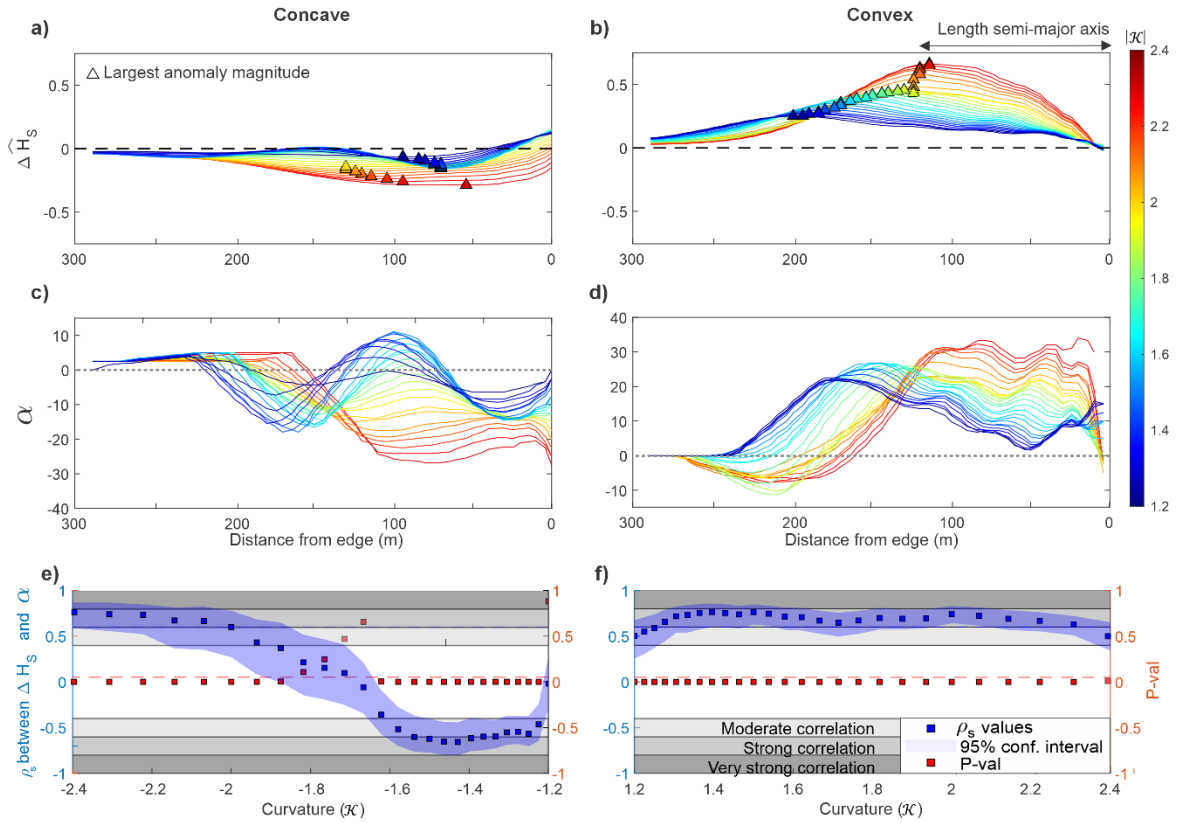


**Figure 3:** Relationship between directional patterns and significant wave height anomalies of non-breaking waves across concave (left) and convex platforms (right) at the centreline ( $y = 150$  m) for different degrees of curvature showing: the significant wave height anomalies (a,b) and the cross-shore directional patterns (c,d). The impact of directional pattern on wave anomaly pattern was assessed using a spearman correlation between the two parameters (e,f).

407

### 408 3.1.2 Broken waves ( $H_0 = 2.0$ m)

409 The spectral evolution of broken waves across concave platforms displayed a complex  
 410 pattern of spectral anomalies (Fig. 4b-e), with a clear amplification of the principal harmonic  
 411 corresponding to SW over the outer platform for degrees of curvature below 1.9 (at  $f_p$ ,  
 412 positive anomalies reached  $1.5 \text{ m}^2 \text{ Hz}^{-1}$  at  $\mathcal{K} = 2.0$  and  $2.4$ , 0 to 150 m from the edge) and a  
 413 clear attenuation of this harmonic for degrees of curvature exceeding 1.9 (at  $f_p$ , negative  
 414 spectral anomaly reached  $-1.2 \text{ m}^2 \text{ Hz}^{-1}$  at  $\mathcal{K} = 1.2$  and  $1.6$ , 0 to 150 m from the edge). These  
 415 differences were related to the amplification of the principal harmonic for edge curvatures  
 416 below 1.9, displaying anomalies reaching up to  $\sim 12 \text{ m}^2 \text{ Hz}^{-1}$  in the vicinity of the concave edge  
 417 sections (0 to -120 m from the edge) before reaching the platform surface (Fig. 4d,e). Over  
 418 convex platforms, the principal harmonic presented the largest amplification (Fig. 4g-j), which

419 intensified over the outer platform with increasing curvature (positive anomaly at  $f_p$  reached  
420  $2.1 \text{ m}^2 \text{ Hz}^{-1}$  at  $\mathcal{K}= 1.2$  and  $4.1 \text{ m}^2 \text{ Hz}^{-1}$  at  $\mathcal{K}= 2.4$ , 0 to 150 m from edge). In contrast, the  
421 amplification of subharmonics within the  $\text{IG}_H$  and  $\text{IG}_L$  frequency bands toward the shoreline  
422 observed along the platform centreline was stronger for low convex edge curvatures than for  
423 high convex edge curvatures (positive anomaly at  $f_{1/5p}$  reached  $0.7 \text{ m}^2 \text{ Hz}^{-1}$  at  $\mathcal{K}= 1.2$  and  $0.5$   
424  $\text{m}^2 \text{ Hz}^{-1}$  at  $\mathcal{K}= 2.4$ , 150 to 300 m from edge).

425 Relationships between edge curvature and mean wave height anomalies across both  
426 platform types were observed (Fig. 4f,k). For anomalies in the WW and SW frequencies, the  
427 mean wave height anomalies of the second and the principal harmonics presented a strong  
428 linear dependence on the degree of edge curvature of concave and convex edges ( $R^2 > 0.90$ ).  
429 In the  $\text{IG}_H$  frequency band, mean wave height anomalies associated with the second  
430 subharmonic were linearly dependent on the curvature across concave platforms ( $R^2 = 0.67$ ).  
431 The mean wave height anomalies associated with the fifth subharmonic in the  $\text{IG}_L$  frequency  
432 band decreased linearly ( $R^2 = 0.94$ ) with curvature over the convex platforms.

433 Variations in edge curvature affected the relative importance of WW, SW,  $\text{IG}_H$  and  $\text{IG}_L$   
434 anomalies across the platforms. For concave platforms, the increase of concave edge  
435 curvature promoted attenuation of all frequency bands, but particularly for WW and SW. For  
436 the harmonic components within the WW and SW frequency bands, the mean wave height  
437 attenuation across concave platforms was negligible for low curvature ( $\overline{\Delta H_{f_{2p}}}$  and  $\overline{\Delta H_{f_p}}$  and  
438 representing less than 1% of  $H_0$  at  $|\mathcal{K}|=1.2$ ) but intensified for high degrees of curvature  
439 ( $\overline{\Delta H_{f_{2p}}}$  and  $\overline{\Delta H_{f_p}}$  representing less than 3% and 6% of  $H_0$  at  $|\mathcal{K}|=2.4$ ). Across the convex  
440 platforms of low curvature ( $1.2 < |\mathcal{K}| < 1.75$ ), the largest amplification of mean wave height  
441 was observed for the principal harmonic ( $\overline{\Delta H_{f_p}}$  representing 4% to 7% of  $H_0$ ), followed by the  
442 fifth subharmonic ( $\overline{\Delta H_{f_{1/5p}}}$  representing 3% to 3.5% of  $H_0$ ). The amplification of the fifth  
443 subharmonic became less important with increasing curvature, while the mean wave height  
444 of the second harmonic was amplified. For convex curvatures exceeding 1.75, the principal  
445 harmonic displayed the largest amplification ( $\overline{\Delta H_{f_p}}$  representing 7% to 10% of  $H_0$ ), followed  
446 by the second harmonic ( $\overline{\Delta H_{f_{2p}}}$  representing 3% to 4% of  $H_0$ ). Thus, the reduction of convex  
447 edge curvature promoted the amplification of  $\text{IG}_L$ , while the increase of convex edge  
448 curvature promoted the amplification of WW and SW.

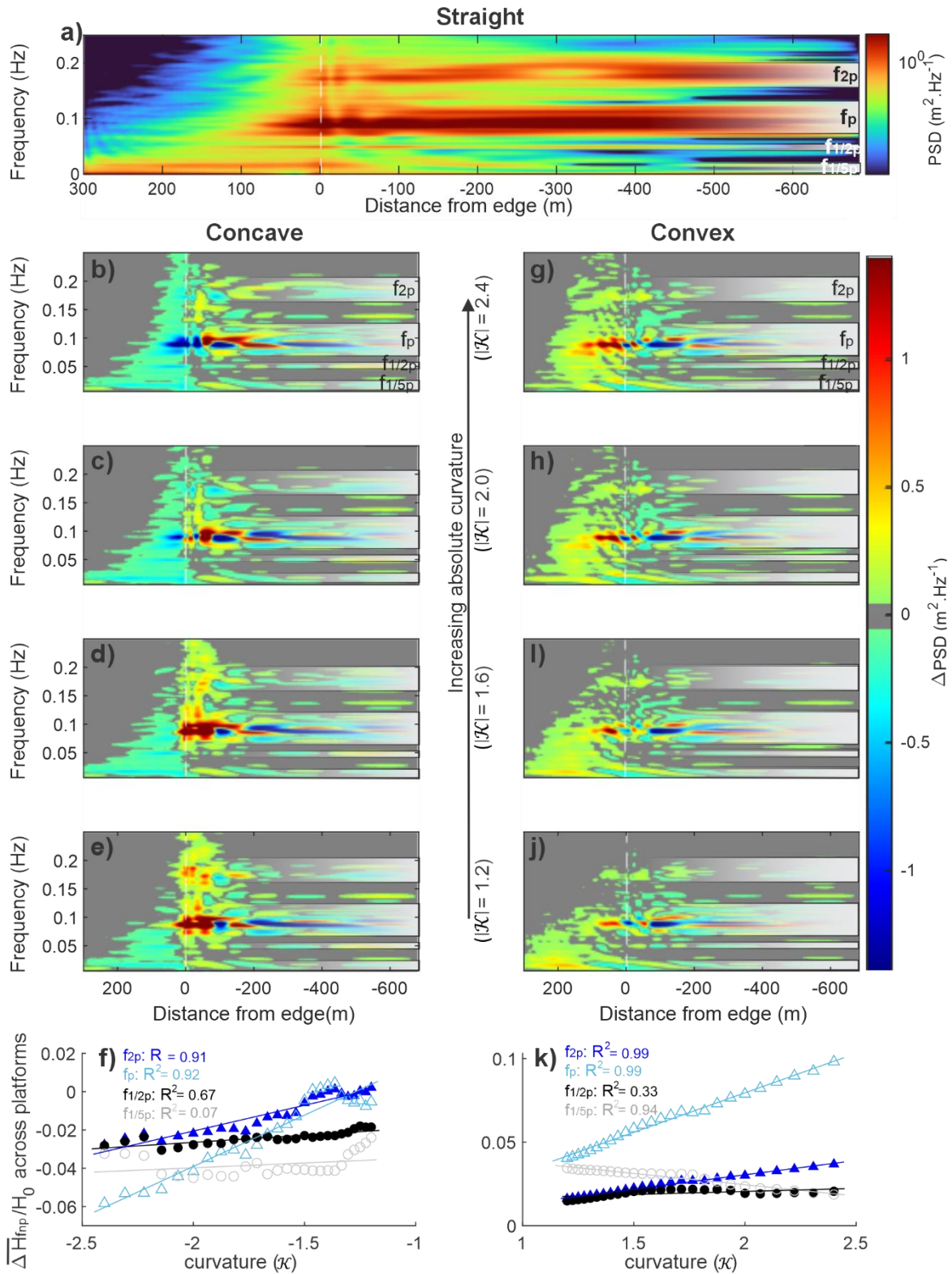


**Figure 4:** Impact of platform edge curvature on the harmonic components of the wavefield for broken waves showing: the spectral anomalies in relation to the straight edge platform (a) for concave platform geometries (b-e) and convex platform geometries (g-j); and the impact of curvature on the mean wave height of each harmonic across the concave (f) and convex (k) platforms.

449

450 The relationship between  $\Delta \widehat{H}_s$  (Fig. 5a,b) and directional patterns (Fig. 5c,d) observed  
451 across the concave and convex platform centrelines was more complex for broken than non-  
452 breaking waves. The main difference with the non-breaking waves resided in the seaward  
453 shift of the maximum divergence (Fig. 5c) and convergence (Fig.5d) locations over the outer  
454 concave and convex platforms, respectively. This shift was particularly pronounced for convex  
455 shore platforms with low degrees of curvature ( $|\mathcal{K}| < 1.8$ ), for which the peaks of convergence  
456 observed mid-platform ( $x \approx 175$  m, Fig. 3d) were attenuated.

457

458

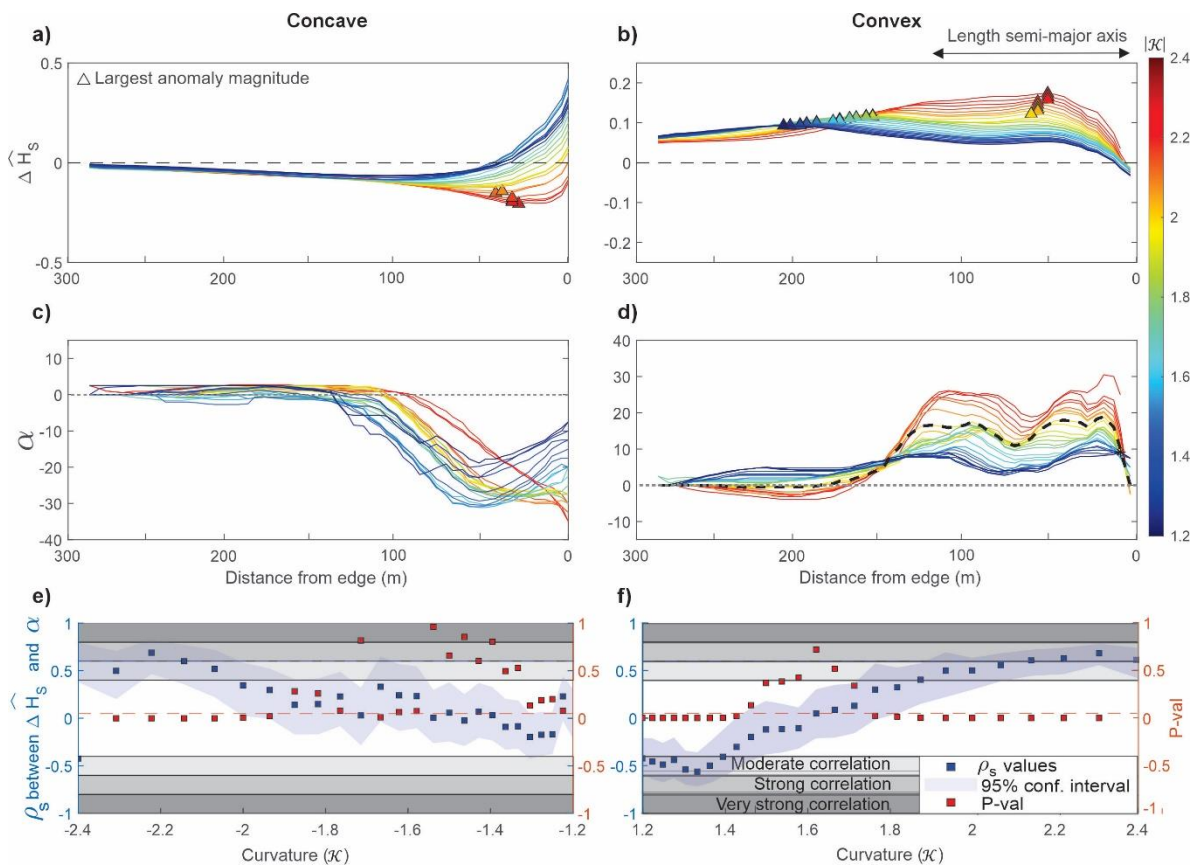


**Figure 5:** Relationship between directional patterns and significant wave height anomalies of broken waves across concave (left) and convex platforms (right) at the centreline ( $y = 150$  m) showing: the significant wave height anomalies (a,b), the cross-shore directional patterns (c,d) and spearman correlation between these two parameters (e,f).

459

460

461

462 For concave platforms, the seaward shift of maximum divergence zones coincided  
463 with a seaward shift of the location of the largest negative anomalies (representing a 25%  
464 attenuation in  $\widehat{H}_s$ , Fig. 5a). As a result, the relationship between  $\Delta\widehat{H}_s$  and directional patterns  
465 of broken waves remained moderate to strong ( $0.4 < \rho_s < 0.6$ ) for concave edge curvatures  
466 exceeding 1.9 (Fig. 5e), indicating that for large degrees of edge curvature, the  $\Delta\widehat{H}_s$  observed  
467 across the concave platform depended on the directional patterns along the centreline. For  
468 convex platforms, the seaward shift of the maximum convergence locations (Fig. 5d)  
469 coincided with a seaward shift of the largest positive anomalies for curvatures over 1.8  
470 (representing an 18% amplification in  $\widehat{H}_s$ , Fig. 5b). However, for curvatures lower than 1.8,  
471 the maximum anomalies shifted landward. Thus, the correlations between  $\Delta\widehat{H}_s$  and  
472 directional patterns across the centreline were moderate to strong ( $0.4 < \rho_s < 0.6$ ) for convex  
473 edge curvatures exceeding 1.8, and weak ( $\rho_s < 0.4$ ) for curvatures dropping below 1.8 (Fig.  
474 5f). This phenomenon can be explained by analysing the relative influence of each harmonic  
475 component on  $\Delta\widehat{H}_s$  observed across the platforms (Fig. 6).

476 For convex curvatures exceeding 1.8, the decrease of wave convergence over the  
477 outer platform and wave ray divergence over the inner platforms (Fig. 5c) coincided with a  
478 reduction of wave height anomalies for all harmonic components over the inner platform (Fig.  
479 6). This reduction was particularly important for the fifth subharmonic,  $\Delta\widehat{H}_{f_{1/5p}}$ , representing  
480 5% of the observed amplification of significant wave height at  $x = 190$  m against 10% at  $x =$   
481  $130$  m for  $|\mathcal{K}|=2.4$ . In contrast, convex edge curvature below 1.8 inhibited the formation of a  
482 divergence zone, ensuring the sustainability of wave ray convergence across the entire  
483 platform. Under these conditions, the wave height anomalies within the WW and SW  
484 frequency bands were sustained across the entire platform, and anomalies within the IG<sub>L</sub>  
485 frequency band were amplified over the inner platform ( $\Delta\widehat{H}_{f_{1/5p}}$  representing 15% of the  
486 observed amplification of normalised significant wave height at  $x = 190$  m for  $|\mathcal{K}|=1.2$ ) to  
487 become the dominant type of anomaly at this location. Thus,  $\Delta\widehat{H}_s$  became predominantly  
488 controlled by the behaviour of IG<sub>L</sub> as curvature decreased ( $1.4 < \mathcal{K} < 1.8$ ). For very low degrees  
489 of curvature ( $\mathcal{K} < 1.4$ ), the amplification of IG<sub>L</sub> was of such importance that  $\Delta\widehat{H}_s$  were

490 amplified over the inner platform despite the decrease in wave convergence, resulting in a  
 491 negative correlation ( $-0.6 < \rho_s < -0.4$ ) between  $\Delta\widehat{H}_s$  and directional patterns (Fig. 5c).

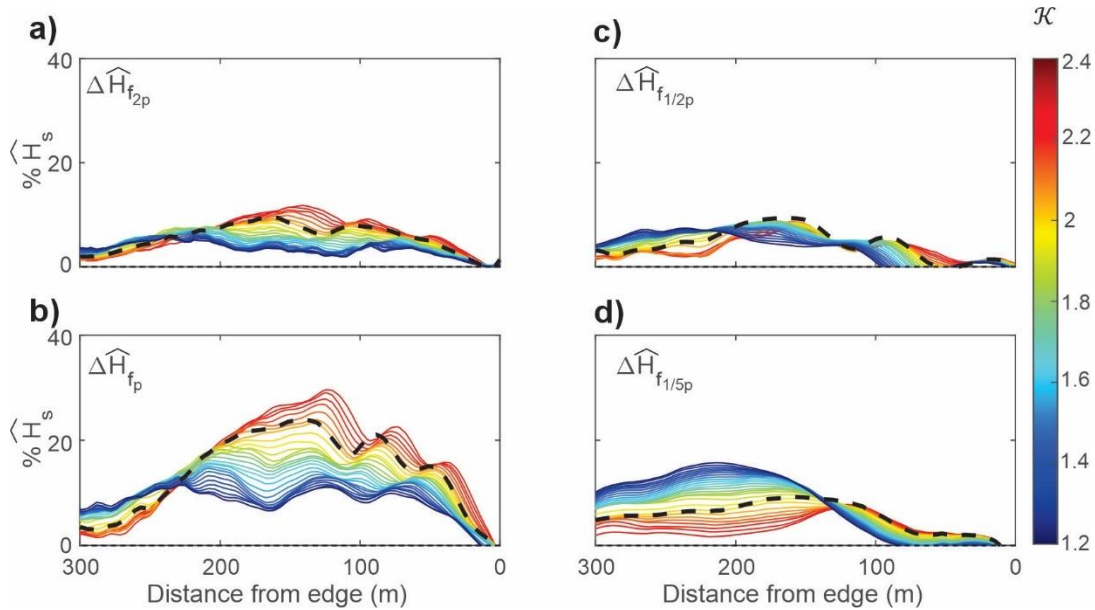


**Figure 6:** Percentage of significant wave height variations across the centreline ( $y = 150$  m) convex platforms associated with anomalies of the second higher harmonics (a), the principal harmonic (b), the second subharmonic (c) and the fifth subharmonic (d) components ( $H_s = H_{sStraight} + \Delta H_s$ ). The dashed line represents a curvature of 1.8, marking the threshold for the formation of a divergence zone over the inner platforms.

492

493

### 494 3.2 Effects of platform edge geometry on alongshore wave height patterns

#### 495 3.2.1 Non-breaking waves

496 Coherent self-interaction maps were plotted to investigate the impact of platform edge  
 497 geometry on alongshore wave height variation over the inner platform for non-breaking  
 498 waves (Fig. 7). Maxima in these maps ( $\widehat{\psi} \approx 1$ ) correspond to areas of strongest coherent  
 499 interaction for the dominant frequency components within the SW and IG<sub>L</sub> frequency bands  
 500 ( $f_p$  and  $f_{1/5p}$ ). Over the concave platforms, zones of coherent self-interaction for the principal  
 501 harmonic ( $f_p$ ) shifted alongshore from the platform centrelines to become concentrated near  
 502 the northern and southern extremities of the platform as the edge curvature increased (Fig.  
 503 7a-d). These alongshore variations were predominantly observed between  $x = 130$  and 175  
 504 m, where divergence along the centreline was the strongest (Fig. 3c). In contrast, coherent

505 self-interaction maps for the fifth subharmonic ( $f_{1/5p}$ ) were more homogenous alongshore  
506 (Fig. 7e-h), except near the shoreline, where coherent self-interactions were predominantly  
507 observed at the platform centreline. Over the convex platform, coherent self-interactions of  
508 the principal harmonic (Fig. 7i-l) were concentrated toward the platform centreline for edge  
509 curvatures between  $|\mathcal{K}|=1.2$  to 1.6 (Fig. 7k,l), but as edge curvature increased, coherent wave  
510 interaction for this harmonic predominantly occurred at the northern and southern  
511 extremities of the platforms (Fig. 7i,j). For the fifth subharmonic, coherent self-interactions  
512 were focussed near the platform centreline for low edge curvature and spread alongshore  
513 toward the shoreline  $|\mathcal{K}|=1.2$  (Fig. 7p). As curvature increased, the areas of fifth subharmonic  
514 coherent self-interactions near the shoreline split into two peaks on either side of the  
515 platform centreline (Fig. 7m,n). This phenomenon was observed at curvatures for which a  
516 mild divergence was observed over the inner platform (Fig. 3d).

517         The wave height distribution over the inner sections of concave and convex platforms  
518 is shown in Fig. 8 and 9. The spatial distribution of the significant wave height ( $\widehat{H}_s$ ) presented  
519 the strongest similitudes ( $R^2 > 0.9$ ) with the wave height patterns of the principal harmonic  
520 ( $\widehat{H}_{fp}$ ) regardless of the platform geometry and curvature. This indicates a strong control of  
521 SW on the patterns of significant wave height variations over the inner platform. In contrast,  
522 the correlation between the wave height patterns of the fifth subharmonic and the significant  
523 wave height patterns over the inner platforms of concave and convex geometries was weak  
524 ( $R^2 < 0.4$ ), indicating that  $IG_L$  had little impact on the variations of significant wave height at  
525 this location.

526

527

528

529

530

531

532

533

534

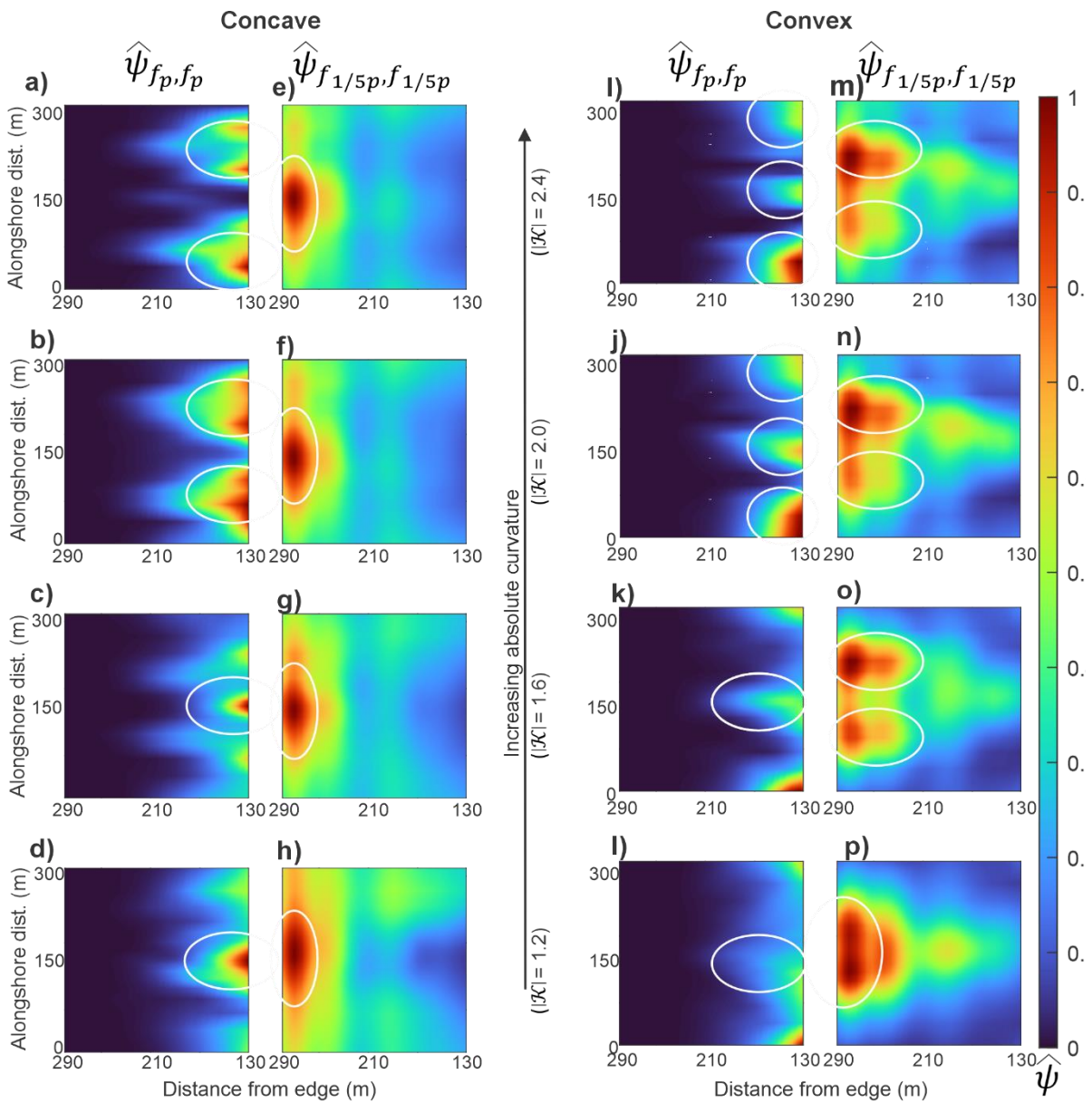


**Figure 7:** Coherent self-interaction maps defined from the bispectral modal state of self-interacting components for the principal harmonic ( $f_p$ ) and the fifth subharmonic ( $f_{1/5p}$ ) of non-breaking waves over the inner platform (Fig. 1) at different concave (a-h) and convex (i-p) edge curvatures. The centreline is located at  $y = 150$  m. Values of  $\hat{\psi}$  of 1 indicate areas of the largest coherent wave interactions. The white ellipses highlight the zones of strong coherent wave interactions.

535

536

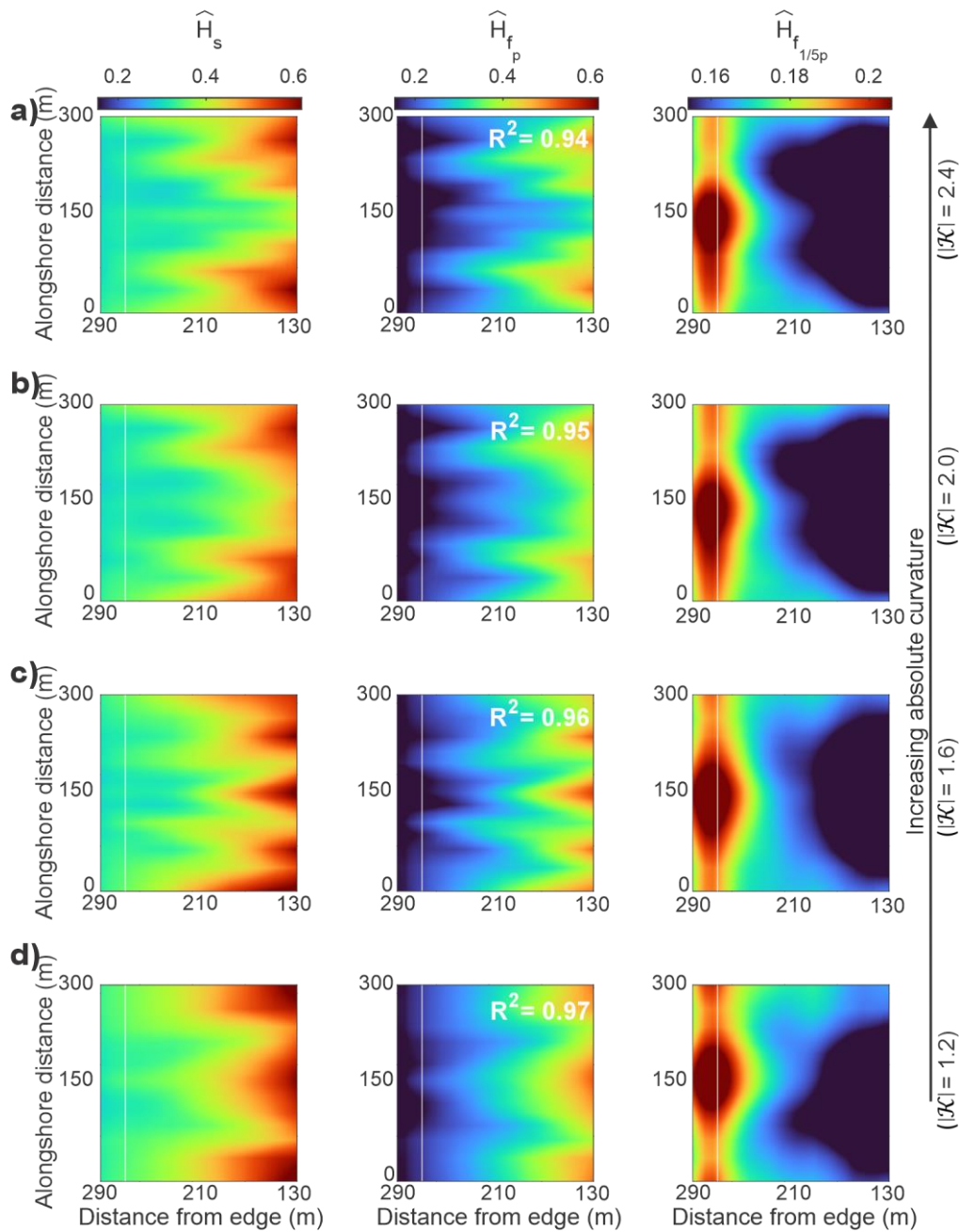


**Figure 8:** Wave height distribution for the entire frequency range ( $\widehat{H}_s$ ), the principal harmonic ( $\widehat{H}_{f_p}$ ) and the fifth subharmonic ( $\widehat{H}_{f_{1/5p}}$ ) of non-breaking waves over the inner platform (Fig. 1) for various concave (a-d) edge curvatures. The white line represents the alongshore transect L, 20 m from the shoreline (Fig. 1). The centreline is located at  $y = 150$  m. The  $R^2$  values indicate the correlation between wave height patterns of the principal harmonic and fifth subharmonic with the significant wave height pattern for the same degree of curvature (only  $R^2 \geq 0.4$  is shown, representing moderate to very strong correlations)

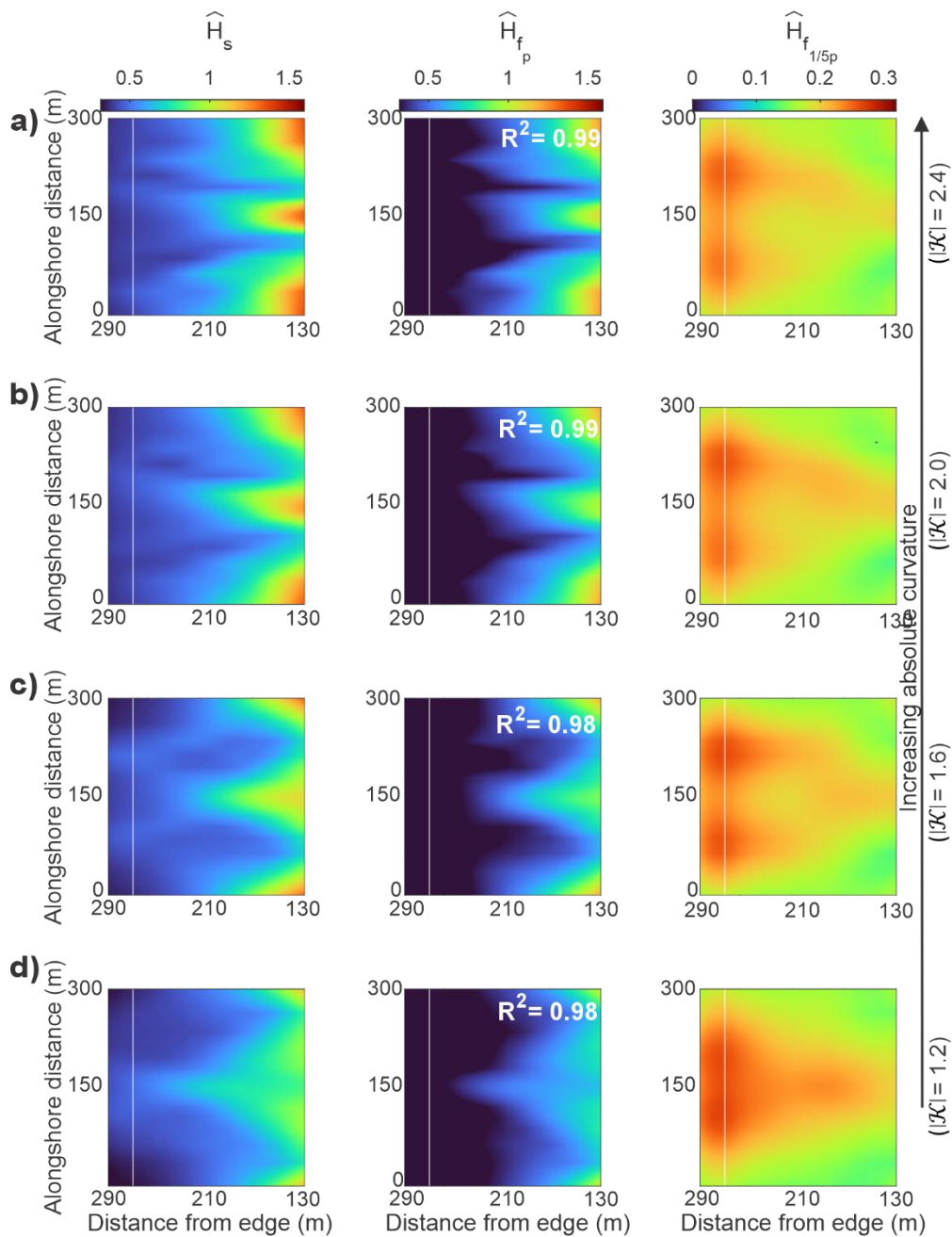


**Figure 9:** Wave height distribution for the entire frequency range ( $\widehat{H}_s$ ), the principal harmonic ( $\widehat{H}_{f_p}$ ) and the fifth subharmonic ( $\widehat{H}_{f_{1/5p}}$ ) of non-breaking waves over the inner platform (Fig. 1) for various convex (a-d) edge curvatures. The white line represents the alongshore transect L, 20 m from the shoreline (Fig. 1). The centreline is located at  $y = 150$  m. The  $R^2$  values indicate the correlation between wave height patterns of the principal harmonic and fifth subharmonic with the significant wave height pattern for the same degree of curvature (only  $R^2 \geq 0.4$  is shown, representing moderate to very strong correlations)

541

542 A strong relationship,  $R^2 > 0.8$ , was observed between modal coherent self-interaction  
 543 patterns and wave height patterns of the principal harmonic and fifth subharmonics over the  
 544 inner sections of concave (Fig. 10a) and convex platforms (Fig. 10b). This observation indicates  
 545 that the alongshore variations of the principal harmonic (SW) were predominantly controlled  
 546 by coherent wave interaction, which in turn drove the alongshore variations in significant  
 547 wave height over the inner section of both concave and convex platforms. The resulting  
 548 stationary patterns in significant wave height along the shoreline were characterised by a  
 549 decrease of significant wave height toward the centreline of concave platforms (Fig. 11a),  
 550 which became more pronounced with increasing curvature (maximum alongshore difference  
 551 in  $\widehat{H}_s=0.05$  at  $|\mathcal{K}|=1.2$ , increasing to 0.06 at  $|\mathcal{K}|=2.4$ , Fig. 10a). Over convex platforms,  
 552 stationary patterns for normalised significant wave height were characterised by an increase  
 553 of significant wave height toward the platform centreline at low degrees of curvature (Fig.  
 554 11b), resulting in an alongshore difference in  $\widehat{H}_s \approx 0.15$  for  $|\mathcal{K}| < 1.8$  near the shoreline. A  
 555 progressive amplification of the lobes on either side of the centreline was observed as  
 556 curvature increased, resulting in a more homogenous alongshore distribution of significant  
 557 wave height for high degrees of curvature ( $\widehat{H}_s \approx 0.06$  for  $|\mathcal{K}| > 2$ , Fig. 11b).

558

559

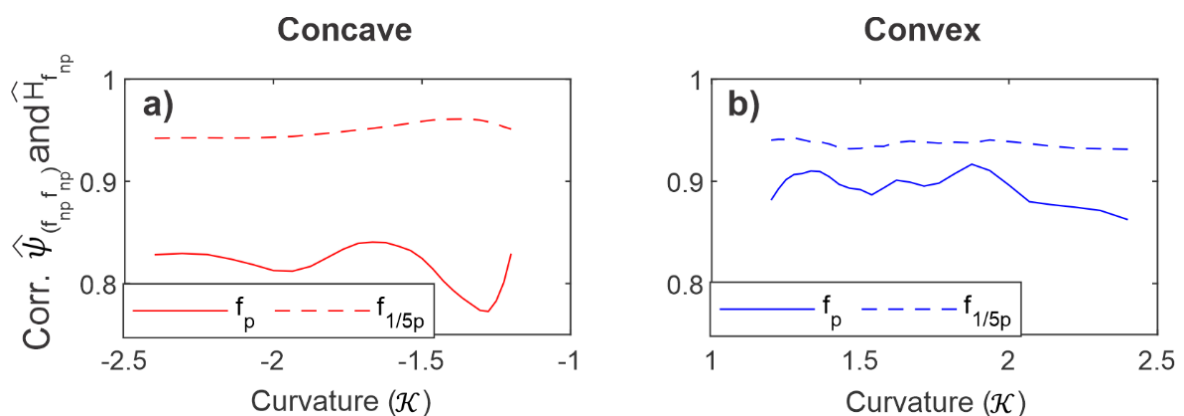


**Figure 10:** Correlation between interaction maps (Fig. 7) and wave height patterns (Fig. 8, 9) for the principal harmonic ( $f_p$ ) and the fifth subharmonic ( $f_{1/5p}$ ) of non-breaking waves over the inner platform of concave (a) and convex (b) edges.

560

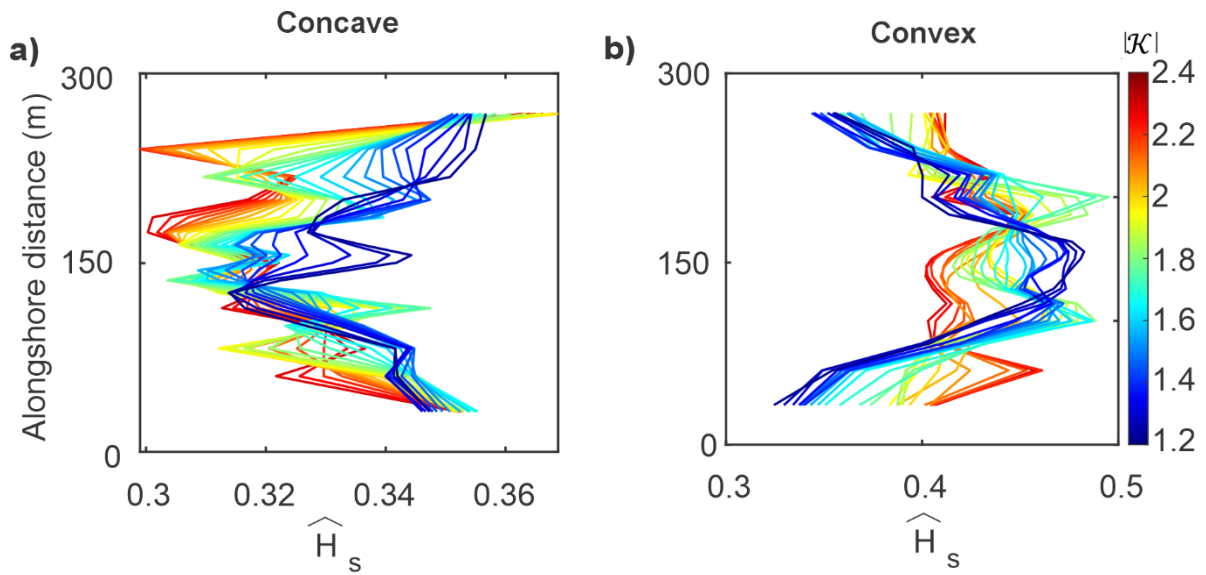


**Figure 11:** Alongshore variations in significant wave height patterns 20 m from the shoreline for non-breaking waves (transect L, Fig. 1) in relation to concave (a) and convex (d) edge curvatures

### 562 3.2.2 Broken waves

563 Coherent self-interaction patterns of the principal harmonic and fifth subharmonic of  
 564 broken waves displayed alongshore variabilities over both concave and convex platforms (Fig.  
 565 12). Over the concave platforms, the coherent self-interaction zone of the principal harmonic  
 566 was concentrated toward the centreline for low degrees of curvature ( $|\mathcal{K}|=1.2$ ), spreading  
 567 alongshore as the degree of curvature increased (Fig. 12a-d). Zones of coherent self-  
 568 interactions for the fifth subharmonic were predominantly observed on the northern and  
 569 southern extremities of the platforms and became more distinct as the edge curvature  
 570 increased (Fig. 12e-h). Over the convex platforms, coherent self-interactions of the principal  
 571 harmonic were the strongest on the northern and southern extremities of the platforms at  
 572  $x \approx 190$  m. For the fifth subharmonic (Fig. 12m-p), areas of coherent self-interaction were  
 573 concentrated along the platform centrelines for low degrees of curvature ( $|\mathcal{K}|=1.2$  and 1.6),  
 574 but spread either side of the platform centrelines for high degrees of curvature ( $|\mathcal{K}|=2.0$  and  
 575 2.4). The differences in coherent self-interaction patterns between low and high degrees of  
 576 curvature were characterised by a mild divergence over the inner section of convex platforms  
 577 for curvatures greater than 1.8 (Fig. 7d).

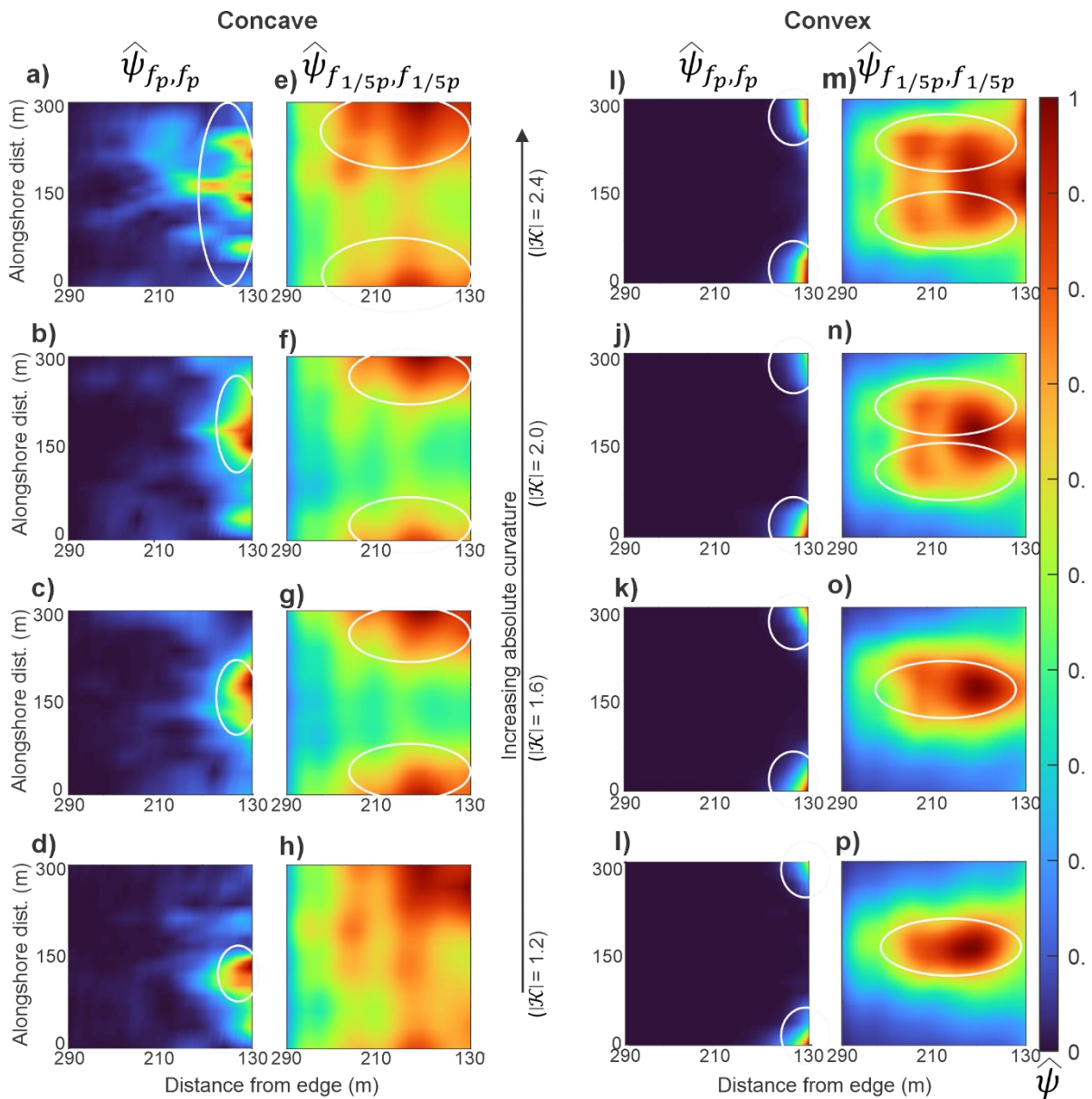


**Figure 12:** Coherent self-interaction maps defined from the bispectral modal state of self-interacting components for the principal harmonics ( $f_p$ ) and the fifth subharmonic ( $f_{1/5p}$ ) of broken waves over the inner platform (Fig. 1) at different concave (a-h) and convex (i-p) edge curvatures. The centreline is located at  $y = 150$  m. Values of  $\hat{\psi}$  of 1 indicate areas of strong coherent wave interactions. The white ellipses highlight the zones of strong coherent wave interactions.

582

583 For broken waves, the influence of  $IG_L$  on significant wave height distribution over the  
584 inner sections of concave and convex platforms was greater than for non-breaking waves (Fig.  
585 13, Fig. 14). Over the inner section of the concave platforms (Fig. 13), the fifth subharmonic  
586 had greater wave height than the principal harmonic. Thus, the wave height patterns of the  
587 fifth subharmonic had a greater impact on the significant wave height patterns ( $0.85 < R^2 <$   
588  $0.91$  for  $1.2 < |\mathcal{K}| < 2.4$ ) than the principal harmonic ( $0.74 < R^2 < 0.86$  for  $1.2 < |\mathcal{K}| < 2.4$ ) in this  
589 region. The wave height of the principal harmonic and fifth subharmonic decreased from the  
590 northern and southern extremities of the platforms to the platform centrelines. The  
591 combined effect of these patterns was a net alongshore decrease of significant wave height  
592 toward the platform centrelines. Over the inner section of convex platforms (Fig. 14), the  
593 principal harmonic displayed the greatest wave height (maximum  $\widehat{H}_{fp} \approx 0.5$ ) on the northern  
594 and southern sides of the platform between  $x \approx 130-190$  m. The wave height of the fifth  
595 subharmonic was relatively smaller, reaching a maximum at the platform centreline  
596 (maximum  $\widehat{H}_{fp} \approx 0.22-0.27$ ), regardless of the curvature. As a result, the wave height  
597 distribution of the principal harmonic exerted a strong control on the significant wave height  
598 pattern over the inner platforms ( $0.9 < R^2 < 0.95$ ) in comparison to the control exerted by the  
599 fifth subharmonic ( $0.4 < R^2 < 0.58$ ). However, the wave height of the principal harmonic  
600 significantly decreased past  $x \approx 190$  m, becoming comparable to the wave height of the fifth  
601 subharmonic. Thus, alongshore variations in significant wave height were controlled by  
602 alongshore patterns of both principal harmonic and fifth subharmonic for  $x \geq 190$  m. For low  
603 degrees of edge curvature ( $|\mathcal{K}|=1.2$ ), the maximum wave height of the fifth subharmonic was  
604 observed at the platforms' centreline and evolved with increasing curvature to form two  
605 maxima on either side of the centreline for large degrees of edge curvature ( $|\mathcal{K}|= 2.2$  and  
606  $2.4$ ). This evolution was clearly observed in the significant wave height pattern between  $x =$   
607  $190$  and  $300$  m, underlining the influence of the fifth subharmonic ( $IG_L$ ) on the alongshore  
608 variation of significant wave height at the shoreline.

609

610

611

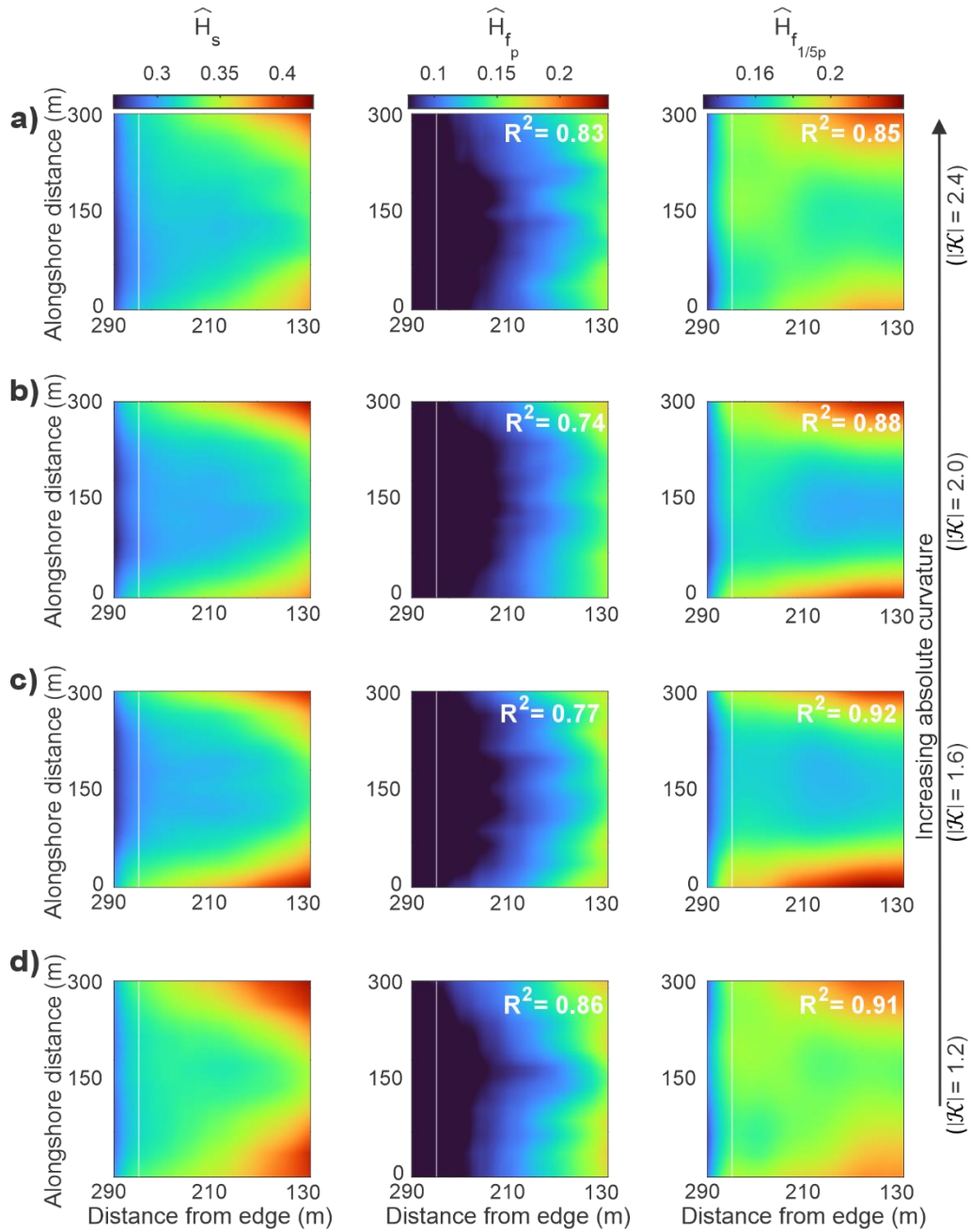


**Figure 13:** Wave height distribution for the entire frequency range ( $\widehat{H}_s$ ), the principal harmonic ( $\widehat{H}_{f_p}$ ) and the fifth subharmonic ( $\widehat{H}_{f_{1/5p}}$ ) of broken waves over the inner platform (Fig. 1) for various concave (a-d) edge curvatures. The white line represents the alongshore transect L, 20 m from the shoreline. The centreline is located at  $y = 150$  m. The  $R^2$  values indicate the correlation between wave height patterns of the principal harmonic and fifth subharmonic with the significant wave height pattern for the same degree of curvature.

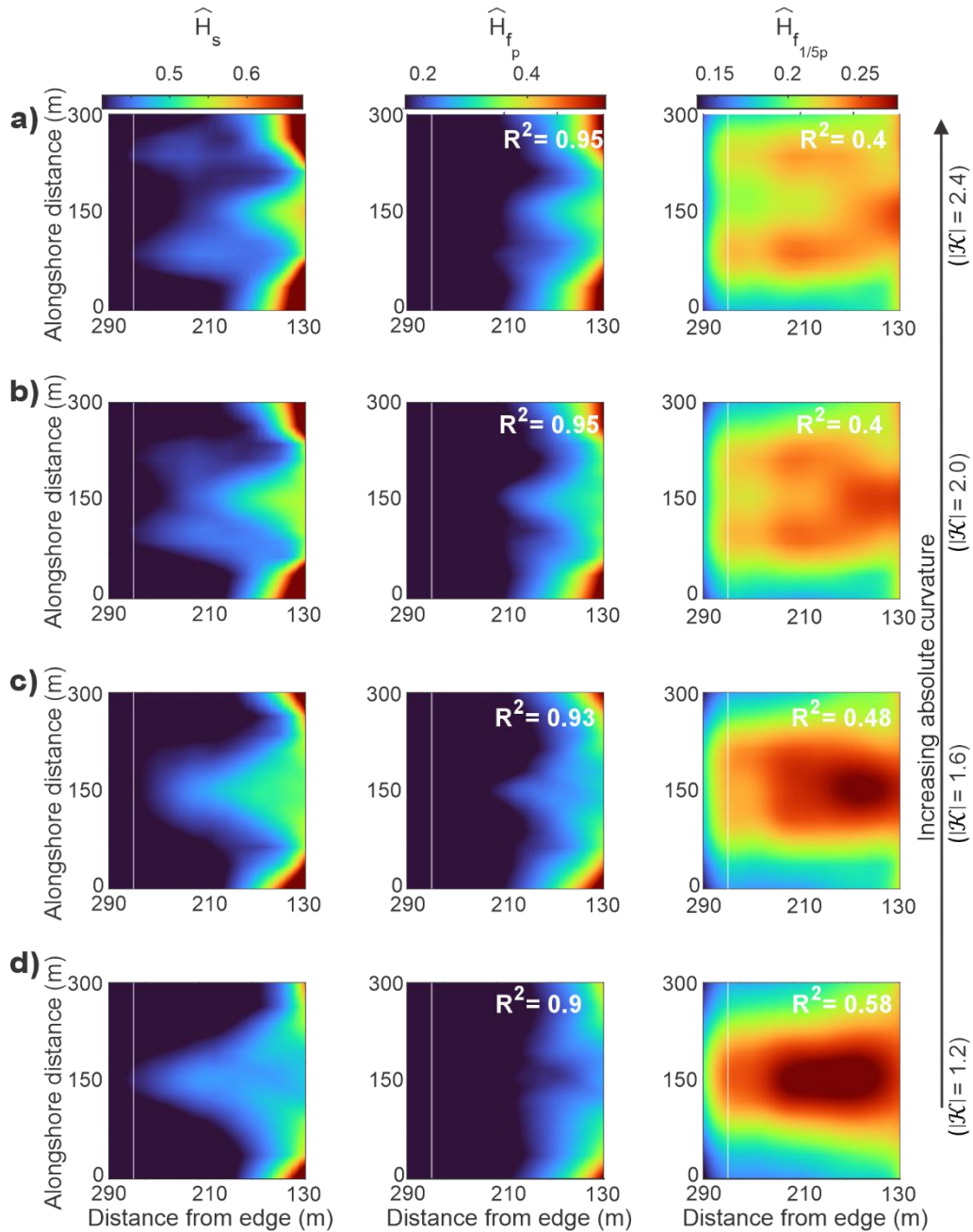


**Figure 14:** Wave height distribution for the entire frequency range ( $\widehat{H}_s$ ), the principal harmonic ( $\widehat{H}_{f_p}$ ) and the fifth subharmonic ( $\widehat{H}_{f_{1/5p}}$ ) of broken waves over the inner platform (Fig. 1) for various convex (a-d) edge curvatures. The white line represents the alongshore transect L, 20 m from the shoreline. The centreline is located at  $y = 150$  m. The  $R^2$  values indicate the correlation between wave height patterns of the principal harmonic and fifth subharmonic with the significant wave height pattern for the same degree of curvature.

613

614

615 Strong ( $R^2 > 0.8$ ) and moderate to strong ( $0.5 < R^2 < 0.7$ ) relationships were observed  
616 over the inner sections of concave (Fig. 15a) and convex platforms (Fig. 15b) between modal  
617 coherent self-interaction patterns and wave height patterns for the fifth subharmonics and  
618 principal harmonics, respectively. The implication is that coherent wave amplification  
619 influenced the longshore patterns of wave height for the principal harmonic and fifth  
620 subharmonic over the inner platform, although this process had a smaller impact on the  
621 principal harmonic. Thus, coherent wave amplification at IG frequencies was the principal  
622 process controlling alongshore variations of significant wave height along the shoreline. The  
623 resulting stationary patterns in significant wave height along the shoreline were marked by a  
624 decrease of significant wave height toward the centreline of concave platforms, which  
625 became more pronounced with increasing curvature (maximum alongshore difference in  
626  $\widehat{H}_s=0.04$  at  $|\mathcal{K}|=1.2$ , increasing to 0.02 at  $|\mathcal{K}|=2.4$ , Fig. 16a). For convex platforms, an increase  
627 of significant wave height toward the platform centreline was observed at low degrees of  
628 curvature, resulting in maximum alongshore variations of significant wave height  $\widehat{H}_s \approx 0.08$   
629 for  $|\mathcal{K}|<1.8$ . A progressive amplification of the lobes on either side of the centreline  
630 generated two wave height maxima for high degrees of curvature, for which maximum  
631 alongshore variations of significant wave height  $\widehat{H}_s \approx 0.06$  for  $|\mathcal{K}|>2$  (Fig. 16b).

632

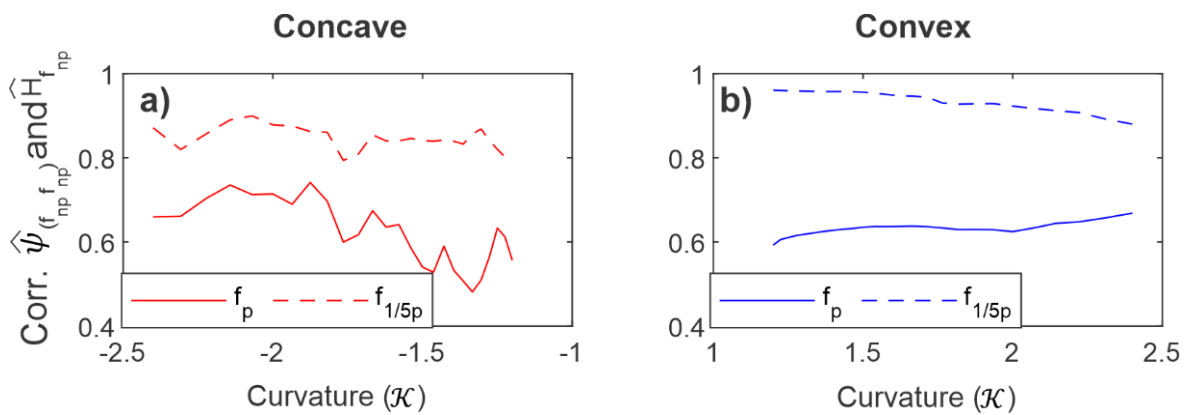


**Figure 15:** Correlation between interaction maps and wave height patterns for the principal harmonic ( $f_p$ ) and the fifth subharmonic ( $f_{1/5p}$ ) of broken waves over the inner platform of concave (a) and convex (b) edges.

633

634

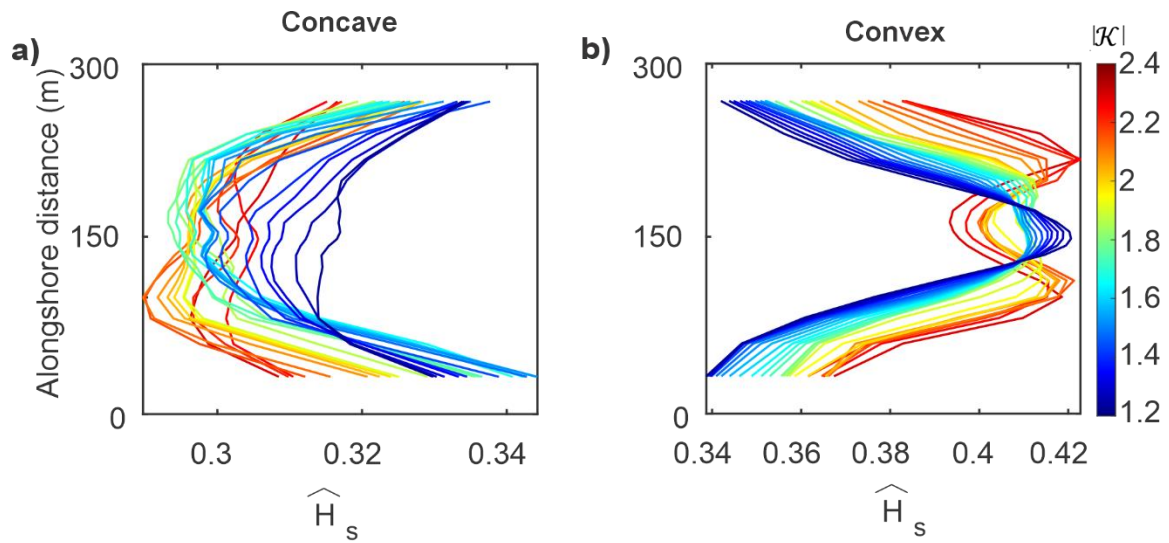


**Figure 16:** Alongshore variations in normalised significant wave height patterns 20 m from the shoreline (transect L) for broken waves in relation to concave (a) and convex (d) curvature.

636

## 637 4 Discussion

### 638 4.1 Impact of platform edge geometry on wave transformation across shore platforms

639 Modelling studies generally investigate the impact of refraction on wave energy  
 640 distribution over a fixed curvature (e.g. Berkhoff et al., 1982; Li et al., 2020), whereas in this  
 641 work, we varied the degree of edge curvature and analysed its effect on the transformation  
 642 of harmonic components. Increasing concave edge curvature decreased the wave energy of  
 643 harmonic components in WW, SW, IG<sub>H</sub> and IG<sub>L</sub> frequency bands (Fig. 2b-e, 4b-e), accounting  
 644 for up to 25% reduction in  $\widehat{H}_s$  (Fig. 3a, 5a). In contrast, increasing convex edge curvature  
 645 amplified both the second and principal harmonics in the WW and SW frequency bands over  
 646 the outer platforms, increasing  $\widehat{H}_s$  by up to 55% and 18% for non-breaking and broken waves  
 647 (Fig. 3b, 5b) while minimizing the amplification of the fifth subharmonic within the IG<sub>L</sub>  
 648 frequency band over the inner platforms (Fig. 2g-j, 4g-j). Thus, it is clear that morphological  
 649 variability in platform edge curvature influences significant wave height on shore platforms,  
 650 and this has potential implications for backwear and downwear erosion processes on rock  
 651 coasts (e.g. Trenhaile, 1987, Matsumoto et al., 2016a,b).

652 Amplification of higher harmonics associated with wave refraction has previously been  
653 associated with wave focusing (Gouin et al., 2017), but the impact of edge curvature on  
654 amplification has not been considered. Our modelling results show that increasing convex  
655 edge curvature enhances wave focussing over the outer platform (Fig. 3, 5), promoting the  
656 generation of higher harmonic from non-linear triadic (sum) interactions (Janssen and  
657 Herbers, 2009; Jarry et al., 2011; Lawrence et al., 2022). Shore platform studies have linked  
658 the generation and dominance of high-frequency waves over the outer section of near-  
659 horizontal platforms to locally generated wind waves (e.g. Ogawa et al., 2011; 2016). Though  
660 this process cannot be ruled out, the nearshore wind speed required for locally produced WW  
661 energy is substantial (Hasselmann et al., 1973), and the generation of higher harmonics from  
662 non-linear triadic interaction caused by wave refraction appears to be a more plausible  
663 physical interpretation for high-frequency wave generation on the outer sections of shore  
664 platforms.

665 Research has demonstrated that wave amplification in the IG frequency band over near-  
666 horizontal platforms is influenced by the ratio of water depth at the cliff toe to the platform  
667 width, and relative submergence (Beetham and Kench, 2011; Ogawa et al., 2015). We show  
668 that edge curvature exerts an additional morphological control on IG amplification across  
669 convex platforms by affecting the balance between focusing intensity from refraction and  
670 defocusing effects from wave breaking controlled by convex edges (Fig. 4, 5). Although a  
671 decrease in convex edge curvature should theoretically result in a landward shift of the focal  
672 point over submerged flats (e.g. Mandlier and Kench, 2012), a seaward shift of the focal point  
673 was observed in this study for broken waves (Fig. 5d). This phenomenon can be attributed to  
674 the defocussing effects resulting from the enhancement of radiation stress and wave-  
675 generated current by wave breaking (Yoon et al., 2004; Choi et al., 2009). A critical curvature  
676 was found for which the intensity of wave focusing by wave refraction is not strong enough  
677 to overcome the defocusing effects of wave breaking, identified here as  $|\mathcal{K}|=1.8$  (Fig. 5d).  
678 When the critical curvature is exceeded, wave rays intersect across the platform centreline,  
679 in which cases, IG amplification is minimised by wave ray divergence over the inner platform  
680 (Fig. 6d). In contrast, for convex edge curvatures lower than the critical curvature, wave rays  
681 do not intersect across the platform centreline, sustaining wave convergence across the  
682 entire platform. In this case, IG amplification is promoted over the inner platform,

683 representing up to 15% of the increase in significant wave height at this position (Fig. 6d).  
684 Thus, the present research identifies convergence as a key mechanism acting on the growth  
685 of IG across shore platform, working in conjunction with other processes such as to  
686 breakpoint forcing (Poate et al., 2020) and energy transfer from higher frequencies and  
687 shoaling (Beetham and Kench, 2011).

688 In a conceptual model, Ogawa et al. (2011) described spatial zones on a shore platform  
689 that are dominated by different wave types and pointed out that the spatial characteristics  
690 change according to the tidal stage. Here, we show that shifts in dominant wave types across  
691 shore platforms are also controlled by convex edge curvature (certainly at high tide). High  
692 convex curvature amplifies harmonics within the WW and SW frequency bands over the outer  
693 platform and inhibits the amplification of IG over the inner platform (Fig. 4g). Low degrees of  
694 convex curvature have the opposite effect (Fig. 4j), resulting in the seaward shift of the zones  
695 dominated by WW and SW frequency bands. The influence of refraction patterns generated  
696 by convex edge geometries on the collective behaviour of harmonics affected the significant  
697 wave height patterns across convex platforms. Baldock et al. (2020) hypothesised that the  
698 significant wave height across convex platforms is defined by a specific balance between  
699 cross-shore energy loss from dissipation and energy gain from oblique refracted SW, resulting  
700 in a correlation between significant wave height anomalies and refraction patterns. The  
701 strong relationship ( $\rho_s > 0.6$ ) observed between directional patterns and significant wave  
702 height anomalies of non-breaking waves (Fig. 3f) suggest that, for this wave state, energy is  
703 effectively gained across the platform from refracted SW. However, for broken waves, the  
704 correlation between directional patterns and significant wave height anomalies ( $\Delta\widehat{H}_s$ )  
705 decreased with curvature to become weak ( $\rho_s < 0.4$ ) below the critical curvature threshold  
706 (Fig. 5f). These differences are attributed to the influence of IG growth on significant wave  
707 height over the inner platform due to the amplification of IG from post-breaking energy  
708 transfer from high to low frequency (Poate et al., 2020), and low sustained convergence  
709 across the platform (Fig. 5b, 6d). These results underline the importance of considering the  
710 refraction patterns of both SW and IG when investigating significant wave height patterns  
711 across convex submerged flats.

712

## 713 4.2 Impact of platform edge geometry on along shore wave transformation

714 Coherent wave amplification is identified here as a crucial process affecting SW and IG<sub>L</sub>  
715 height distribution in the inner section of near-horizontal platforms. For non-breaking waves,  
716 the dominant frequencies within both SW and IG<sub>L</sub> frequency bands presented strong  
717 correlations between patterns of coherent wave interaction and wave height distribution  
718 over concave and convex platforms (Fig. 10). However, this correlation decreased for the  
719 principal harmonic in the SW frequency bands in the presence of wave breaking (Fig. 15),  
720 perhaps due to the combination of defocussing (Yoon et al., 2004) and dissipation effects  
721 (Farrell et al., 2009) associated with wave breaking.

722 The present observations validate the hypothesis of Winter et al. (2017) on the  
723 formation of alongshore stationary IG patterns from wave refraction over convex platforms.  
724 However, our results suggest that such patterns are generated by coherent wave interaction  
725 following the generation of caustic rays in the IG<sub>L</sub> frequency band (Fig. 7m-p, 12m-p) rather  
726 than alongshore standing waves, as Winter et al. (2017) suggested. In fact, the latter would  
727 require interacting IG to propagate alongshore in opposite directions. The directional analysis  
728 presented here precludes such a possibility ( $\alpha \approx 0^\circ$  near the shoreline, Fig. 3, 5). As the  
729 present paper demonstrates the coherent wave interaction plays crucial role in alongshore IG  
730 wave patterns, a coherent wave class should be added to the resonant, progressive-  
731 dissipative, standing and progressive-growing low-frequency wave classes previously  
732 identified over submerged flats (Gawehn et al., 2016).

733 The combined modes of SW and IG coherent wave amplification exerted a crucial  
734 control on the stationary patterns of significant wave heights over the inner platform. For  
735 non-breaking waves, significant wave height variations over the inner platform are  
736 predominantly controlled by coherent wave amplification of SW (Fig. 7, 8). In contrast, for  
737 breaking waves, the distribution of significant wave height over the inner platform became  
738 controlled by coherent wave amplification occurring within both SW and IG<sub>L</sub> frequency  
739 components as IG<sub>L</sub> became a prominent wave type in this region (Ogawa et al. 2011) (Fig. 13,  
740 14). The present results support the conceptual model presented by Krier-Mariani et al.  
741 (2022), suggesting that patterns of wave ray intersection on either side of concave edge  
742 sections result in stationary SW and IG amplification patterns. The control exerted by the

743 critical curvature on the alongshore distribution of SW and IG over convex platforms can be  
744 attributed to the generation of a terminal point (marking the transition from wave ray  
745 convergence to divergence) at the platform centreline for convex curvatures exceeding the  
746 critical curvature. In such cases, caustic rays are formed on either side of the centreline  
747 (Mandlier and Kench, 2012), promoting coherent wave interactions in these regions (Fig. 12a,  
748 14a).

749 It follows that the control exerted by platform curvature on coherent wave  
750 amplification plays an essential role in the nodal state of significant wave height along the  
751 shoreline (Fig. 11, 16). For concave platforms, a node near the centreline and antinodes on  
752 the northern and southern extremities of the platform were observed. For convex edge  
753 curvature under the critical curvature threshold, an antinode was observed along the  
754 platform centreline where waves converged, while for curvature exceeding the critical  
755 curvature threshold, two antinodes were observed on either side of the platform centreline.  
756 While such patterns could wrongly be associated with edge waves, the present results  
757 support the observations of Dalrymple (1975), who first associated nodal and anti-nodal  
758 points in alongshore wave height patterns with coherent wave interaction.

759 It has previously been established that by controlling the nodal state of significant wave  
760 height along the shoreline of open coasts, coherent wave amplification could lead to the  
761 formation of rip currents (Dalrymple, 1975; Wei and Dalrymple, 2017). This mechanism is  
762 expected to impact circulation patterns over near-horizontal platforms equally. da Silva et al.  
763 (2023) identified alongshore pressure gradient as the dominant driver of circulation patterns  
764 in the lee of submerged flats, resulting in two or four-cell circulation systems. A two-cell  
765 system is typically characterised by an alongshore diverging flow from the lee of the  
766 submerged flat edge to the shoreline, while a four-cell system is characterised by an  
767 alongshore diverging flow at the lee of the submerged flat and a converging flow at the  
768 shoreline. Considering the present results, it can be hypothesised that stationary wave  
769 patterns and the subsequent alongshore pressure gradient generated by coherent wave  
770 amplification drive the formation of circulation cells over convex platforms. Theoretically, the  
771 formation of two antinodes over the inner platform would result in a four-cell circulation  
772 system (Fig. 14a,b, Fig. 16b), while an antinode across the entire platform would result in a

773 two-cell circulation system (Fig. 14c,d, Fig.16b). These differences depend on whether or not  
774 the submerged flat geometry allows for the formation of a terminal point. Previous studies  
775 established that this condition was predominantly controlled by the distance between the  
776 seaward edge of submerged flats and the shoreline (da Silva et al., 2022, 2023; Ranasinghe et  
777 al., 2006, 2010), while we show that the degree of edge curvature is equally important (Fig.  
778 11, 16).

## 779 **5 Conclusions**

780 This study employed an exploratory numerical modelling approach to investigate the  
781 impact of concave and convex platform edge geometries on the behaviour of wave harmonics  
782 and the subsequent wave height distribution patterns over near-horizontal shore platforms.  
783 Harmonic analyses show that refraction patterns controlled by concave and convex platform  
784 edge curvatures result in wave height variation for the principal and second higher harmonics  
785 over the outer platform, and for the subharmonics over the inner platform. Wave divergence  
786 across concave edge platforms decreased the height of harmonics within both SW and IG  
787 frequency bands, resulting in the attenuation of significant wave height for high degrees of  
788 curvature. Over the outer section of convex platforms, increasing curvature intensified wave  
789 focusing and amplified the principal and second harmonics within the SW frequency band. A  
790 critical curvature value of 1.8 demarcates the formation of a wave ray divergence zone over  
791 the inner platform, conditioned by the balance between wave focusing from wave refraction  
792 and wave defocusing from wave breaking. Below this threshold, wave convergence amplified  
793 IG over the inner platform, but over this threshold, wave divergence reduced the  
794 amplification of IG over the inner platform. Through these mechanisms, it is apparent that  
795 edge curvature can influence both the relative dominance of SW and IG frequencies, and the  
796 pattern of significant wave height transformation across near-horizontal platforms. Using a  
797 high-order spectral decomposition method, this study further demonstrated that coherent  
798 wave amplification influences stationary IG and SW patterns over the inner platform,  
799 affecting the alongshore distribution of significant wave height. We found that platform  
800 geometry controls the nodal state of the stationary patterns along the shoreline, possibly  
801 resulting in alongshore variation of wave erosive force and the generation of wave-generated  
802 currents shaping rock coasts.

## 803        **Acknowledgements**

804                . RKM is supported by a University of Otago PhD Scholarship and a New Zealand  
805 Coastal Society Student Research Scholarship. Mark Dickson and Wayne Stephenson are  
806 supported by a Royal Society Te Apārangi, Marsden Fund Grant Number UOO1828. We are  
807 grateful for the assistance and support provided by Callum Walley and the rest of the team  
808 from NeSi for allowing us to set up and run our models on their supercomputer facilities.

809

## 810        **Open research**

811                The numerical model input files and post processed data for the model simulations  
812 (Using FUNWAVE 3.6) over idealised shore platform geometries are available at *Public release*  
813 *planned after review.*

## 814        **References**

- 815 Baldock, T.E., Shabani, B., Callaghan, D.P., Hu, Z., Mumby, P.J., 2020. Two-dimensional modelling of  
816 wave dynamics and wave forces on fringing coral reefs. *Coast. Eng.* 155, 103594.  
817 <https://doi.org/10.1016/j.coastaleng.2019.103594>
- 818 Beetham, E.P., Kench, P.S., 2011. Field observations of infragravity waves and their behaviour on  
819 rock shore platforms. *Earth Surf. Process. Landforms* 36, 1872–1888.  
820 <https://doi.org/10.1002/esp.2208>
- 821 Berkhoff, J.C.W., Booy, N., Radder, A.C., 1982. Verification of numerical wave propagation models  
822 for simple harmonic linear water waves. *Coast. Eng.* 6, 255–279. [https://doi.org/10.1016/0378-3839\(82\)90022-9](https://doi.org/10.1016/0378-3839(82)90022-9)
- 824 Blenkinsopp, C.E., Chaplin, J.R., 2008. The effect of relative crest submergence on wave breaking  
825 over submerged slopes. *Coast. Eng.* 55, 967–974.  
826 <https://doi.org/10.1016/j.coastaleng.2008.03.004>
- 827 Buckley, M.L., Lowe, R.J., Hansen, J.E., Van Dongeren, A.R., 2015. Dynamics of wave setup over a  
828 steeply sloping fringing reef. *J. Phys. Oceanogr.* 45, 3005–3023. <https://doi.org/10.1175/JPO-D-15-0067.1>
- 830 Buckley, M.L., Lowe, R.J., Hansen, J.E., Van Dongeren, A.R., Storlazzi, C.D., 2018. Mechanisms of  
831 wave-driven water level variability on reef-fringed coastlines. *J. Geophys. Res. Ocean.* 123,  
832 3811–3831. <https://doi.org/10.1029/2018JC013933>
- 833 Chen, Q., Dalrymple, R.A., Kirby, J.T., Kennedy, A.B., Haller, M.C., 1999. Boussinesq modeling of a rip  
834 current system. *J. Geophys. Res. Ocean.* 104, 20617–20637.  
835 <https://doi.org/10.1029/1999jc900154>
- 836 Chen, Q., Kirby, J.T., Dalrymple, R.A., Shi, F., Thornton, E.B., 2003. Boussinesq modeling of longshore  
837 currents. *J. Geophys. Res.* 108, 1–18. <https://doi.org/10.1029/2002JC001308>

- 838 Choi, J., Lim, C.H., Lee, J.I., Yoon, S.B., 2009. Evolution of waves and currents over a submerged  
839 laboratory shoal. *Coast. Eng.* 56, 297–312. <https://doi.org/10.1016/j.coastaleng.2008.09.002>
- 840 Dalrymple, R.A., 1975. A mechanism for Rip Current Generation on an open Coast. *J. Geophys. Res.*  
841 80, 3485–3487.
- 842 da Silva, R. F., Hansen, J. E., Lowe, R. J., Rijnsdorp, D. P., & Buckley, M. L., 2023. Dynamics of the  
843 wave-driven circulation in the lee of nearshore reefs. *Journal of Geophysical Research: Oceans*,  
844 128, e2022JC019013. <https://doi.org/10.1029/2022JC019013>
- 845 da Silva, R. F., Hansen, J. E., Rijnsdorp, D. P., Lowe, R. J., & Buckley, M. L. 2022. The influence of  
846 submerged coastal structures on nearshore flows and wave runup. *Coastal Engineering*, 177,  
847 104194. <https://doi.org/10.1016/j.coastaleng.2022.104194>
- 848 Emery, W.J., Thomson, R.E., 2014. *Time-series Analysis Methods, Data Analysis Methods in*  
849 *Physical Oceanography*. Elsevier, Amsterdam. [https://doi.org/10.1016/b978-044450756-](https://doi.org/10.1016/b978-044450756-3/50006-x)  
850 [3/50006-x](https://doi.org/10.1016/b978-044450756-3/50006-x)
- 851 Falk, L., 1979. On The Phase Integral Of Coherent Three-wave Interaction. *Phys. Lett.* 71, 61–62.
- 852 Farrell, E.J., Granja, H., Cappiotti, L., Ellis, J.T., Li, B., Sherman, D.J., 2009. Wave transformation across  
853 a rock platform, Belinho, Portugal. *J. Coast. Res.* 44–48.
- 854 Gawehn, M., Van Dongeren, A., Van Rooijen, A., Storlazzi, C.D., Cheriton, O.M., Reniers, A., 2016.  
855 Identification and classification of very low frequency waves on a coral reef flat. *J. Geophys.*  
856 *Res. Ocean.* 121, 3010–3028. <https://doi.org/10.1002/2016JC011834>.Received
- 857 Guoin, M., Ducrozet, G., Ferrant, P., 2017. Propagation of 3D non-linear waves over an elliptical  
858 mound with a High-Order Spectral method. *Eur. J. Mech. B/Fluids* 63, 9–24.  
859 <https://doi.org/10.1016/j.euromechflu.2017.01.002>
- 860 Gottlieb, S., Shu, C.-W., Tadmor, E., 2001. Strong stability-preserving high-order time discretization  
861 methods. *SIAM Review* 43, 89–112.
- 862 Griffiths, L.S., Porter, R., 2012. Focusing of surface waves by variable bathymetry. *Appl. Ocean Res.*  
863 34, 150–163. <https://doi.org/10.1016/j.apor.2011.08.004>
- 864 Harid, V., Gołkowski, M., Bell, T., Li, J.D., Inan, U.S., 2014. Finite difference modeling of coherent  
865 wave amplification in the Earth’s radiation belts. *Geophys. Res. Lett.* 41, 8193–8200.  
866 <https://doi.org/10.1002/2014GL061787>
- 867 Hashimoto, N., Nagai, T., Asai, T., 1994. Extension of the Maximum Entropy Principle Method for  
868 Directional Wave Spectrum Estimation, in: *Coastal Engineering Proceedings*. pp. 232–246.  
869 <https://doi.org/10.1061/9780784400890.019>
- 870 Hasselmann, K., Barnett, T.P., Bouws, E., Carlson, H., Cartwright, D.E., Enke, K., Ewing, J.A., Gienapp,  
871 H., Hasselmann, D.E., Kruseman, P., Meerburg, A., Muller, P., Olbers, D.J., Richter, K., Sell, W.,  
872 Walden, H., 1973. Measurements of wind-wave growth and swell decay during the Joint North  
873 Sea Wave Project (JONSWAP). UDO 551.466.31; ANE German Bight, Deutsches  
874 Hydrographisches Institut Hamburg.
- 875 Hasselmann, K., Munk, W.H., MacDonald, G., 1963. Bispectra of Ocean Waves, in: Rosenblatt, M.  
876 (Ed.), *Symposium on Time Series Analysis*. pp. 125–139.
- 877 Inouye, S., Pfau, T., Gupta, S., Chikkatur, A.P., Görlitz, A., Pritchard, D.E., Ketterle, W., 1999. Phase-  
878 coherent amplification of atomic matter waves. *Nature* 402, 641–644.

- 879 <https://doi.org/10.1038/45194>
- 880 Ito, Y., Tanimoto, K., 1972. A Method of Numerical Analysis of Wave Propagation-Application To  
881 Wave Diffraction and Refraction. Proc. 13Th. Coast. Engng. Conf., (Vancouver, Canada) 1, 503–  
882 522. <https://doi.org/10.9753/icce.v13.25>
- 883 Janssen, T.T., Herbers, T.H.C., 2009. Non-linear wave statistics in a focal zone. J. Phys. Oceanogr. 39,  
884 1948–1964. <https://doi.org/10.1175/2009JPO4124.1>
- 885 Jarry, N., Rey, V., Gouaud, F., Lajoie, D., 2011. Gravity wave amplification and phase crest re-  
886 organization over a shoal. Nat. Hazards Earth Syst. Sci. 11, 789–796.  
887 <https://doi.org/10.5194/nhess-11-789-2011>
- 888 Kennedy, A.B., Kirby, J.T., Chen, Q., Dalrymple, R.A., 2001. Boussinesq-type equations with improved  
889 non-linear performance. Wave Motion 33, 225–243. [https://doi.org/10.1016/S0165-  
890 2125\(00\)00071-8](https://doi.org/10.1016/S0165-2125(00)00071-8)
- 891 Kim, Y.C., Powers, E.J., 1979. Digital Bispectral Analysis and Its Applications to Non-linear Wave  
892 Interactions. IEEE Trans. Plasma Sci. 7, 120–131. <https://doi.org/10.1109/TPS.1979.4317207>
- 893 Kozuma, M., Suzuki, Y., Torii, Y., Sugiura, T., Kuga, T., Hagley, E., Deng, L., 1999. Phase-Coherent  
894 Amplification of Matter Waves. Science (80-. ). 286, 2309–2312.
- 895 Stephenson, W.J., Kirk, R.M., 2000a. Development of shore platforms on Kaikoura Peninsula ,  
896 South Island , New Zealand Part One : The role of waves. Geomorphology 32, 21–41.
- 897 Krier-Mariani, R.L., Stephenson, W.J., Wakes, S.J., Dickson, M.E., 2023. The effects of platform  
898 morphology on two-dimensional wave transformation over near-horizontal shore platforms.  
899 Geomorphology 422, 108555. <https://doi.org/10.1016/j.geomorph.2022.108555>
- 900 Krier-Mariani, R.L., Stephenson, W.J., Wakes, S.J., Dickson, M.E., 2022. Perspectives on wave  
901 transformation over a near-horizontal shore platform: Comparison of a two-dimensional and  
902 transect approach. Geomorphology 405, 108200.  
903 <https://doi.org/10.1016/j.geomorph.2022.108200>
- 904 Lawrence, C., Trulsen, K., Gramstad, O., 2022. Extreme wave statistics of surface elevation and  
905 velocity field of gravity waves over a two-dimensional bathymetry. J. Fluid Mech. 939, 1–18.  
906 <https://doi.org/10.1017/jfm.2022.227>
- 907 Li, C.Y., Shih, R.S., Weng, W.K., 2020. Investigation of ocean-wave-focusing characteristics induced by  
908 a submerged crescent-shaped plate for long-crested waves. Water 12, 1–17.  
909 <https://doi.org/10.3390/w12020509>
- 910 Lumley, J.L. 1967. The Structure of Inhomogeneous Turbulent Flows. In: Yaglom, A.M. and Tartarsky,  
911 V.I., Eds., Atmospheric Turbulence and Radio Wave Propagation, 166-177.
- 912 Lynett, P., Liu, P.L.F., 2004. A two-layer approach to wave modelling. Proc. R. Soc. A Math. Phys. Eng.  
913 Sci. 460, 2637–2669. <https://doi.org/10.1098/rspa.2004.1305>
- 914 Mandlier, P.G., Kench, P.S., 2012. Analytical modelling of wave refraction and convergence on coral  
915 reef platforms: Implications for island formation and stability. Geomorphology 159–160, 84–92.  
916 <https://doi.org/10.1016/j.geomorph.2012.03.007>
- 917 Marshall, R.J.E., Stephenson, W.J., 2011. The morphodynamics of shore platforms in a micro-tidal  
918 setting: Interactions between waves and morphology. Mar. Geol. 288, 18–31.  
919 <https://doi.org/10.1016/j.margeo.2011.06.007>

- 920 Matsumoto, H., Dickson, M.E., Kench, P.S., 2016a. An exploratory numerical model of rocky shore  
 921 profile evolution. *Geomorphology* 268, 98–109.  
 922 <https://doi.org/10.1016/j.geomorph.2016.05.017>
- 923 Matsumoto, H., Dickson, M.E., Kench, P.S., 2016b. Modelling the Development of Varied Shore  
 924 Profile Geometry on Rocky Coasts Modelling the Development of Varied Shore Profile  
 925 Geometry on Rocky Coasts. *J. Coast. Res.* 75(sp1), 597–601. <https://doi.org/10.2112/S175-120.1>
- 926 Mendonca, A., Neves, M. G. and Fortes, C. J., 2008. Numerical Study of Hydrodynamics around an  
 927 artificial surf reef for São Pedro do Estoril, Portugal, SI 56 (Proceedings of the 10th International  
 928 Coastal Symposium), 1010 – 1014. Lisbon, Portugal, ISSN 0749-0258.
- 929 Ogawa, H., Dickson, M.E., Kench, P.S., 2016. Generalised observations of wave characteristics on  
 930 near-horizontal shore platforms: Synthesis of six case studies from the North Island, New  
 931 Zealand. *N. Z. Geog.* 72, 107–121. <https://doi.org/10.1111/nzg.12121>
- 932 Ogawa, H., Dickson, M.E., Kench, P.S., 2015. Hydrodynamic constraints and storm wave  
 933 characteristics on a sub-horizontal shore platform. *Earth Surf. Process. Landforms* 40, 65–77.  
 934 <https://doi.org/10.1002/esp.3619>
- 935 Ogawa, H., Dickson, M.E., Kench, P.S., 2011. Wave transformation on a sub-horizontal shore  
 936 platform , Tatapouri , North Island , New Zealand. *Cont. Shelf Res.* 31, 1409–1419.  
 937 <https://doi.org/10.1016/j.csr.2011.05.006>
- 938 Pequignet, A.-C.N., Becker, J.M.B., Merrifield, M.A.M., 2014. Energy transfer between wind waves  
 939 and low-frequency oscillations on a fringing reef, Ipan, Guam Anne-Christine. *J. Geophys. Res.*  
 940 *Ocean.* 3868–3882. <https://doi.org/10.1002/2014JC010179>.Received
- 941 Poate, T., Masselink, G., Austin, M.J., Inch, K., Dickson, M., McCall, R., 2020. Infragravity wave  
 942 generation on shore platforms: Bound long wave versus breakpoint forcing. *Geomorphology*  
 943 350, 1–15. <https://doi.org/10.1016/j.geomorph.2019.106880>
- 944 Priestley, M.B. 1981: *Spectral Analysis and Time Series*. Academic Press, London.
- 945 Ranasinghe, R., Larson, M., & Savioli, J., 2010. Shoreline response to a single shore-parallel  
 946 submerged breakwater. *Coastal Engineering*, 57(11–12), 1006–1017.  
 947 <https://doi.org/10.1016/j.coastaleng.2010.06.002>
- 948 Ranasinghe, R., Turner, I. L., & Symonds, G., 2006. Shoreline response to multi-functional artificial  
 949 surfing reefs: A numerical and physical modelling study. *Coastal Engineering*, 53(7), 589–611.  
 950 <https://doi.org/10.1016/j.coastaleng.2005.12.004>
- 951 Schmidt, O.T., 2020. Bispectral mode decomposition of non-linear flows. *Non-linear Dyn.* 102, 2479–  
 952 2501. <https://doi.org/10.1007/s11071-020-06037-z>
- 953 Sheremet, A., Kaihatu, J.M., Su, S.F., Smith, E.R., Smith, J.M., 2011. Modeling of non-linear wave  
 954 propagation over fringing reefs. *Coast. Eng.* 58, 1125–1137.  
 955 <https://doi.org/10.1016/j.coastaleng.2011.06.007>
- 956 Shi, F., Kirby, J.T., Harris, J.C., Geiman, J.D., Grilli, S.T., 2012. A high-order adaptive time-stepping TVD  
 957 solver for Boussinesq modeling of breaking waves and coastal inundation. *Ocean Model.* 43–  
 958 44, 36–51. <https://doi.org/10.1016/j.ocemod.2011.12.004>
- 959 Shi, F., Kirby, J.T., Tehranirad, B., Harris, C.H., Choi, Y., Malej, M., 2016. FUNWAVE-TVD. Fully Non-  
 960 linear Boussinesq Wave Model with TVD Solver. Documentation and User 's Manual (Version  
 961 3.0). Research Report NO. CACR-11-03 CENTER, Center of Applied Coastal Research, University

962 of Delaware.

963 Stephenson, W.J., Kirk, R.M., 2000. Development of shore platforms on Kaikoura Peninsula ,  
964 South Island , New Zealand Part One : The role of waves. *Geomorphology* 32, 21–41.

965 Su, S., Ma, G., Hsu, T., 2021. Numerical modeling of low-frequency waves on a reef island in the  
966 South China Sea during typhoon events. *Coast. Eng.* 169, 103979.  
967 <https://doi.org/10.1016/j.coastaleng.2021.103979>

968 Su, S. F., Ma, G., & Hsu, T. W., 2015. Boussinesq modeling of spatial variability of infragravity waves  
969 on fringing reefs. *Ocean Engineering*, 101, 78–92.  
970 <https://doi.org/10.1016/j.oceaneng.2015.04.022>

971 Sunamura, T., 1992. *Geomorphology of Rock Coast*. John Wiley & Sons, Chichester, 102, 139-183

972 Tamura, H., Kawaguchi, K., Fujiki, T., 2020. Phase-Coherent Amplification of Ocean Swells Over  
973 Submarine Canyons. *J. Geophys. Res. Ocean.* 125, 1–16. <https://doi.org/10.1029/2019jc015301>

974 Thomas, T.J., Dwarakish, G.S., 2015. Numerical Wave Modelling – A Review. *Aquat. Procedia* 4, 443–  
975 448. <https://doi.org/10.1016/j.aqpro.2015.02.059>

976 Thompson, C.F., Dickson, M.E., Young, A.P., 2022. Seismic signatures of individual wave impacts on a  
977 coastal cliff. *Earth Surf. Process. Landforms* 1–13. <https://doi.org/10.1002/esp.5426>

978 Thompson, C.F., Young, A.P., Dickson, M.E., 2019. Wave impacts on coastal cliffs: Do bigger waves  
979 drive greater ground motion? *Earth Surf. Process. Landforms* 44, 2849–2860.  
980 <https://doi.org/10.1002/esp.4712>

981 Thornton, E.B., Guza, R.T., 1983. Transformation of Wave Height Distribution. *J. Geophys. Res.* 88,  
982 5925–5938.

983 Tonelli, M., Petti, M., 2009. Hybrid finite volume - finite difference scheme for 2DH improved  
984 Boussinesq equations. *Coast. Eng.* 56, 609–620.  
985 <https://doi.org/10.1016/j.coastaleng.2009.01.001>

986 Trenhaile, A.S., 2000. Modeling the development of wave-cut shore platforms. *Mar. Geol.* 166, 163–  
987 178.

988 Trenhaile, A.S., 1999. The width of shore platforms in Britain, Canada, and Japan. *J. Coast. Res.* 15,  
989 355–364.

990 Trenhaile, A.S., 1987. *The Geomorphology of Rock Coasts*. Oxford University Press, Oxford, 25, 384.

991 Tsujimoto, H., 1987. Dynamic conditions for shore platform initiation, Science Report  
992 of the Institute of Geoscience.

993 Wei, Z., Dalrymple, R.A., 2017. SPH Modeling of Short-crested Waves, in: *Coastal Engineering*  
994 *Proceedings*.

995 Wei, G., Kirby, J.T., Sinha, A., 1999. Generation of waves in Boussinesq models using a source  
996 function method. *Coast. Eng.* 271–299.

997 Weiland, J., Wilhelmsson, H., 1977. *Coherent non-linear interaction of wave in plasmas*, Pergamon,  
998 Oxford

999 Welch, P.D., 1967. The Use of Fast Fourier Transform for the Estimation of Power Spectra: A Method  
1000 Based on Time Averaging Over Short, Modified Periodograms. *IEEE Trans. Audio*  
1001 *Electroacoust.* AU-15, 70–73.

1002 Winter, G.R.J., Lowe, G., Symonds, J.E.H., Van Dongeren, A.R., 2017. Standing infragravity waves over  
1003 an alongshore irregular rocky bathymetry. *J. Geophys. Res. Ocean.* 122, 4868–4885.  
1004 <https://doi.org/10.1002/2016JC012264>.Received

1005 Yoon, S.B., Cho, Y.S., Lee, C., 2004. Effects of breaking-induced currents on refraction-diffraction of  
1006 irregular waves over submerged shoal. *Ocean Eng.* 31, 633–652.  
1007 <https://doi.org/10.1016/j.oceaneng.2003.07.008>

1008 Young, T., 1802. *On the Theory of Light and Colours*. *Philos. Trans. R. Soc. London* 12–48.

1009 Zhang, S. J., Zhu, L. S., Zou, K., 2019. A comparative study of numerical models for wave propagation  
1010 and setup on steep coral reefs. *China Ocean Eng.*, 33(4): 424–435, doi: 10.1007/s13344-019-  
1011 0040-6

1012

1013